

# Planck Intermediate Results. X. Physics of the hot gas in the Coma cluster

Planck Collaboration: P. A. R. Ade<sup>88</sup>, N. Aghanim<sup>60</sup>, M. Arnaud<sup>75</sup>, M. Ashdown<sup>72,5</sup>, F. Atrio-Barandela<sup>18</sup>, J. Aumont<sup>60</sup>, C. Baccigalupi<sup>87</sup>, A. Balbi<sup>35</sup>, A. J. Banday<sup>95,8</sup>, R. B. Barreiro<sup>68</sup>, J. G. Bartlett<sup>1,69</sup>, E. Battaner<sup>97</sup>, K. Benabed<sup>61,92</sup>, A. Benoît<sup>58</sup>, J.-P. Bernard<sup>8</sup>, M. Bersanelli<sup>32,50</sup>, A. Bonaldi<sup>70</sup>, J. R. Bond<sup>7</sup>, J. Borrill<sup>13,90</sup>, F. R. Bouchet<sup>61,92</sup>, H. Bourdin<sup>35</sup>, M. L. Brown<sup>70</sup>, C. Burigana<sup>49,34</sup>, P. Cabella<sup>36</sup>, J.-F. Cardoso<sup>76,1,61</sup>, P. Carvalho<sup>5</sup>, A. Catalano<sup>77,74</sup>, L. Cayón<sup>29</sup>, L.-Y. Chiang<sup>64</sup>, G. Chon<sup>81</sup>, P. R. Christensen<sup>84,37</sup>, E. Churazov<sup>80,89</sup>, D. L. Clements<sup>56</sup>, S. Colafrancesco<sup>46</sup>, L. P. L. Colombo<sup>22,69</sup>, A. Coulais<sup>74</sup>, B. P. Crill<sup>69,85</sup>, F. Cuttaia<sup>49</sup>, A. Da Silva<sup>11</sup>, H. Dahle<sup>66,10</sup>, L. Danese<sup>87</sup>, R. J. Davis<sup>70</sup>, P. de Bernardis<sup>31</sup>, G. de Gasperis<sup>35</sup>, A. de Rosa<sup>49</sup>, G. de Zotti<sup>45,87</sup>, J. Delabrouille<sup>1</sup>, F.-X. Désert<sup>53</sup>, C. Dickinson<sup>70</sup>, J. M. Diego<sup>68</sup>, K. Dolag<sup>96,80</sup>, H. Dole<sup>60,59</sup>, S. Donzelli<sup>50</sup>, O. Doré<sup>69,9</sup>, U. Dörl<sup>80</sup>, M. Douspis<sup>60</sup>, X. Dupac<sup>40</sup>, T. A. Enßlin<sup>80</sup>, H. K. Eriksen<sup>66</sup>, F. Finelli<sup>49</sup>, I. Flores-Cacho<sup>8,95</sup>, O. Forni<sup>95,8</sup>, M. Frailis<sup>47</sup>, E. Franceschi<sup>49</sup>, M. Frommert<sup>17</sup>, S. Galeotta<sup>47</sup>, K. Ganga<sup>1</sup>, R. T. Génova-Santos<sup>67</sup>, M. Giard<sup>95,8</sup>, M. Gilfanov<sup>80,89</sup>, J. González-Nuevo<sup>68,87</sup>, K. M. Górski<sup>69,99</sup>, A. Gregorio<sup>33,47</sup>, A. Gruppuso<sup>49</sup>, F. K. Hansen<sup>66</sup>, D. Harrison<sup>65,72</sup>, S. Henrot-Versillé<sup>73</sup>, C. Hernández-Monteagudo<sup>12,80</sup>, S. R. Hildebrandt<sup>9</sup>, E. Hivon<sup>61,92</sup>, M. Hobson<sup>5</sup>, W. A. Holmes<sup>69</sup>, A. Hornstrup<sup>16</sup>, W. Hovest<sup>80</sup>, K. M. Huffenberger<sup>98</sup>, G. Hurier<sup>77</sup>, T. R. Jaffe<sup>95,8</sup>, T. Jagemann<sup>40</sup>, W. C. Jones<sup>24</sup>, M. Juvela<sup>23</sup>, E. Keihänen<sup>23</sup>, R. Kneissl<sup>39,6</sup>, J. Knoche<sup>80</sup>, L. Knox<sup>26</sup>, M. Kunz<sup>17,60</sup>, H. Kurki-Suonio<sup>23,43</sup>, G. Lagache<sup>61</sup>, A. Lähteenmäki<sup>2,43</sup>, A. Lasenby<sup>5,72</sup>, C. R. Lawrence<sup>69</sup>, M. Le Jeune<sup>1</sup>, R. Leonardi<sup>40</sup>, P. B. Lilje<sup>66,10</sup>, M. Linden-Vørnle<sup>16</sup>, M. López-Caniego<sup>68</sup>, P. M. Lubin<sup>27</sup>, J. F. Macías-Pérez<sup>77</sup>, B. Maffei<sup>70</sup>, D. Maino<sup>32,50</sup>, N. Mandolesi<sup>49,4</sup>, M. Maris<sup>47</sup>, F. Marleau<sup>63</sup>, E. Martínez-González<sup>68</sup>, S. Masi<sup>31</sup>, M. Massardi<sup>48</sup>, S. Matarrese<sup>30</sup>, F. Matthai<sup>80</sup>, P. Mazzotta<sup>35\*</sup>, S. Mei<sup>42,94,9</sup>, A. Melchiorri<sup>31,51</sup>, J.-B. Melin<sup>15</sup>, L. Mendes<sup>40</sup>, A. Mennella<sup>32,50</sup>, S. Mitra<sup>55,69</sup>, M.-A. Miville-Deschénes<sup>60,7</sup>, A. Moneti<sup>61</sup>, L. Montier<sup>95,8</sup>, G. Morgante<sup>49</sup>, D. Munshi<sup>88</sup>, J. A. Murphy<sup>83</sup>, P. Naselsky<sup>84,37</sup>, P. Natoli<sup>34,3,49</sup>, H. U. Nørgaard-Nielsen<sup>16</sup>, F. Noviello<sup>70</sup>, S. Osborne<sup>91</sup>, F. Pajot<sup>60</sup>, D. Paoletti<sup>49</sup>, O. Perdereau<sup>73</sup>, F. Perrotta<sup>87</sup>, F. Piacentini<sup>31</sup>, M. Piat<sup>1</sup>, E. Pierpaoli<sup>22</sup>, R. Piffaretti<sup>75,15</sup>, S. Plaszczynski<sup>73</sup>, E. Pointecouteau<sup>95,8</sup>, G. Polenta<sup>3,46</sup>, N. Ponthieu<sup>60,53</sup>, L. Popa<sup>62</sup>, T. Poutanen<sup>43,23,2</sup>, G. W. Pratt<sup>75</sup>, S. Prunet<sup>61,92</sup>, J.-L. Puget<sup>60</sup>, J. P. Rachen<sup>20,80</sup>, R. Rebolo<sup>67,14,38</sup>, M. Reinecke<sup>80</sup>, M. Remazeilles<sup>60,1</sup>, C. Renault<sup>77</sup>, S. Ricciardi<sup>49</sup>, T. Riller<sup>80</sup>, G. Rocha<sup>69,9</sup>, M. Roman<sup>1</sup>, C. Rosset<sup>1</sup>, M. Rossetti<sup>32,50</sup>, J. A. Rubiño-Martín<sup>67,38</sup>, B. Rusholme<sup>57</sup>, M. Sandri<sup>49</sup>, G. Savini<sup>86</sup>, B. M. Schaefer<sup>93</sup>, D. Scott<sup>21</sup>, G. F. Smoot<sup>25,79,1</sup>, F. Stivoli<sup>52</sup>, R. Sudiwala<sup>88</sup>, R. Sunyaev<sup>80,89</sup>, D. Sutton<sup>65,72</sup>, A.-S. Suur-Uiski<sup>23,43</sup>, J.-F. Sygnet<sup>61</sup>, J. A. Tauber<sup>41</sup>, L. Terenzi<sup>49</sup>, L. Toffolatti<sup>19,68</sup>, M. Tomasi<sup>50</sup>, M. Tristram<sup>73</sup>, J. Tuovinen<sup>82</sup>, M. Türler<sup>54</sup>, G. Umana<sup>44</sup>, L. Valenziano<sup>49</sup>, B. Van Tent<sup>78</sup>, J. Varis<sup>82</sup>, P. Vielva<sup>68</sup>, F. Villa<sup>49</sup>, N. Vittorio<sup>35</sup>, L. A. Wade<sup>69</sup>, B. D. Wandelt<sup>61,92,28</sup>, N. Welikala<sup>60</sup>, S. D. M. White<sup>80</sup>, D. Yvon<sup>15</sup>, A. Zacchei<sup>47</sup>, S. Zaroubi<sup>71</sup>, and A. Zonca<sup>27</sup>

(Affiliations can be found after the references)

Received ; accepted

## ABSTRACT

We present an analysis of *Planck* satellite data on the Coma Cluster observed via the Sunyaev-Zeldovich effect. Thanks to its great sensitivity, *Planck* is able, for the first time, to detect SZ emission up to  $r \approx 3 \times R_{500}$ . We test previously proposed spherically symmetric models for the pressure distribution in clusters against the azimuthally averaged data. In particular, we find that the Arnaud et al. (2010) “universal” pressure profile does not fit Coma, and that their pressure profile for merging systems provides a good fit of the data only at  $r < R_{500}$ : by  $r = 2 \times R_{500}$  it underestimates the observed y profile by a factor of  $\approx 2$ . This may indicate that at these larger radii either i) the cluster SZ emission is contaminated by unresolved SZ sources along the line of sight or ii) the pressure profile of Coma is higher at  $r > R_{500}$  than the mean pressure profile predicted by the simulations used to constrain the models. The *Planck* image shows significant local steepening of the y profile in two regions about half a degree to the west and to the south-east of the cluster centre. These features are consistent with the presence of shock fronts at these radii, and indeed the western feature was previously noticed in the ROSAT PSPC mosaic by Markevitch (2000) as well as in the radio. Using *Planck* y profiles extracted from corresponding sectors we find pressure jumps of  $4.5_{-0.1}^{+2.5}$  and  $4.9_{-0.2}^{+0.7}$  in the west and southeast, respectively. Assuming Rankine-Hugoniot pressure jump conditions, we deduce that the shock waves should propagate with Mach number  $M_w = 1.95_{-0.02}^{+0.45}$  and  $M_{se} = 2.03_{-0.04}^{+0.14}$  in the West and Southeast, respectively. Finally, we find that the y and radio-synchrotron signals are quasi-linearly correlated on Mpc scales with small intrinsic scatter. This implies either that the energy density of cosmic-ray electrons is relatively constant throughout the cluster, or that the magnetic fields fall off much more slowly with radius than previously thought.

**Key words.** Cosmology: observations – Galaxies: cluster: general – Galaxies: clusters: intracluster medium – Cosmic background radiation, X-rays: galaxies: clusters

## 1. Introduction

The Coma cluster is the most spectacular Sunyaev-Zeldovich (SZ) source in the *Planck* sky. It is a low-redshift, massive, and hot cluster and is sufficiently extended that *Planck* can resolve

it well spatially. Its intracluster medium (ICM) was observed in SZ for the first time with the 5.5 m OVRO telescope (Herbig et al. 1992, 1995). Later, it was also observed with MSAM1 (Silverberg et al. 1997), MITO (De Petris et al. 2002), VSA (Lancaster et al. 2005) and WMAP (Komatsu et al. 2011) which detected the cluster with a signal-to-noise ratio of  $S/N = 3.6$ . As reported in the all-sky early Sunyaev-Zeldovich cluster pa-

\* Corresponding author: P. Mazzotta, [mazzotta@roma2.infn.it](mailto:mazzotta@roma2.infn.it)

per, *Planck* detected the Coma cluster with a  $S/N > 22$  (Planck Collaboration 2011d).

Coma has also been extensively observed in the X-rays from the ROSAT all-sky survey and pointed observations (Briel et al. 1992; White et al. 1993), as well as via a huge mosaic by XMM-Newton (e.g. Neumann et al. 2001, 2003; Schuecker et al. 2004). The X-ray emission reveals many spatial features indicating infalling sub-clusters such as NGC4839 (Dow & White 1995; Vikhlinin et al. 1997; Neumann et al. 2001, 2003), turbulence (e.g. Schuecker et al. 2004; Churazov et al. 2012) and further signs of accretion and strong dynamical activity.

Moreover, the Coma cluster hosts a remarkable giant radio halo extending over 1 Mpc, which traces the non-thermal emission from relativistic electrons and magnetic fields (e.g. Giovannini et al. 1993; Brown & Rudnick 2011). The radio halo's spectrum and extent require an ongoing, distributed mechanism for acceleration of the relativistic electrons, since their radiative lifetimes against synchrotron and inverse Compton losses are short, even compared to their diffusion time across the cluster. (e.g. Sarazin 1999; Brunetti et al. 2001). The radio halo also appears to exhibit a shock front in the West, also seen in the X-ray image, and is connected at larger scales with a huge radio relic in the Southwest (Ensslin et al. 1998; Brown & Rudnick 2011).

In this paper we present a detailed radial and sector analysis of the Coma cluster as observed by *Planck*. These results are compared with X-ray and radio observations obtained with *XMM-Newton* and the Westerbork Synthesis Radio Telescope.

We use  $H_0 = 70 \text{ km s}^{-1} \text{ Mpc}^{-1}$ ,  $\Omega_m = 0.3$  and  $\Omega_\Lambda = 0.7$ , which imply a linear scale of  $27.7 \text{ kpc arcmin}^{-1}$  at the distance of the Coma cluster ( $z = 0.023$ ). All the maps are in Equatorial J2000 coordinates.

## 2. The *Planck* frequency maps

*Planck*<sup>1</sup> (Tauber et al. 2010; Planck Collaboration 2011a) is the third-generation space mission to measure the anisotropy of the cosmic microwave background (CMB). It observes the sky in nine frequency bands covering 30–857 GHz with high sensitivity and angular resolution from  $31'$  to  $5'$ . The Low Frequency Instrument (LFI; Mandolesi et al. 2010; Bersanelli et al. 2010; Mennella et al. 2011) covers the 30, 44, and 70 GHz bands with amplifiers cooled to 20 K. The High Frequency Instrument (HFI; Lamarre et al. 2010; Planck HFI Core Team 2011a) covers the 100, 143, 217, 353, 545, and 857 GHz bands with bolometers cooled to 0.1 K. Polarisation is measured in all but the highest two bands (Leahy et al. 2010; Rosset et al. 2010). A combination of radiative cooling and three mechanical coolers produces the temperatures needed for the detectors and optics (Planck Collaboration 2011b). Two data processing centres (DPCs) check and calibrate the data and make maps of the sky (Planck HFI Core Team 2011b; Zacchei et al. 2011). *Planck*'s sensitivity, angular resolution, and frequency coverage make it a powerful instrument for galactic and extragalactic astrophysics as well as cosmology. Early astrophysics results are given in Planck Collaboration (2011h–z).

This paper is based on the *Planck* nominal survey of 14 months. The whole sky has been covered two times. We refer

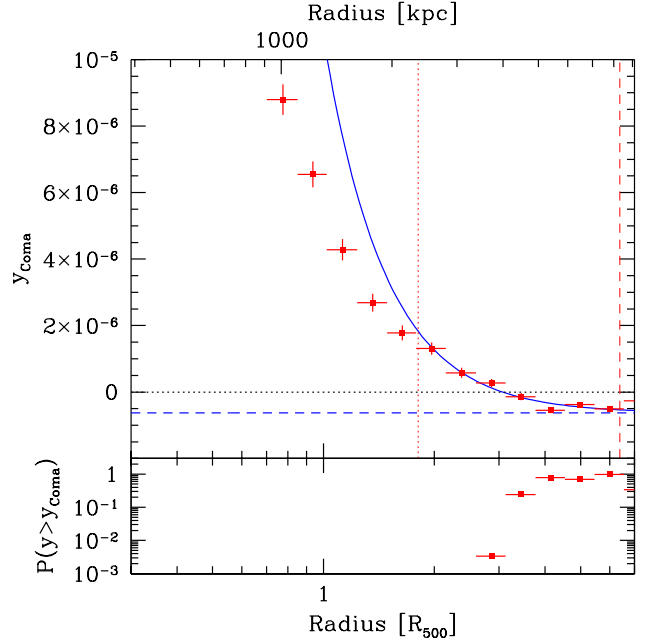


Fig. 1: *Upper panel*: Radial profile of  $y$  in a set of circular annuli centered on Coma. The blue curve is the best fitting simple model to the profile over the radial range from 85 arcmin to 300 arcmin. The model consists of a power-law plus a constant  $y_{\text{off}}$ . The best fitting value of  $y_{\text{off}}$  is shown with the dashed horizontal line. Two vertical lines indicate the range of radii used for fitting. *Lower panel*: The probability of finding an observed value of  $y = y_{\text{Coma}}$  in a given annulus. The probability was estimated by measuring  $y$  in a set of annuli with random centers in any part of the image outside  $5 R_{500}$ . For the annulus between 2.6 and  $3.1 R_{500}$  (or 122 arcmin to 147 arcmin) the probability of getting  $y_{\text{Coma}}$  by chance is  $\sim 3 \times 10^{-3}$  (see Fig. 1). For smaller radii, the probability is much lower, while at larger radii the probability of getting  $y$  in excess of  $y_{\text{Coma}}$  is  $\sim 10\%$  or higher. The results suggest that *Planck* detects the signal from Coma in narrow annuli  $\Delta R/R = 0.2$  at least up to  $R_{\text{max}} \sim 3 R_{500}$ . This is a conservative and model independent estimate.

to Planck HFI Core Team (2011b) and Zacchei et al. (2011) for the generic scheme of time ordered information (TOI) processing and map making, as well as for the technical characteristics of the maps used. We adopt a circular Gaussian beam pattern for each frequency as described in these papers. We use the full-sky maps in the nine *Planck* frequency bands provided in HEALPix (Górski et al. 2005)  $n_{\text{side}}=2048$  resolution. An error map is associated with each frequency band and is obtained from the difference of the first half and second half of the *Planck* rings for a given position of the satellite. The resulting maps are basically free from astrophysical emission. However, they are a good representation of the statistical instrumental noise and systematic error. Uncertainties in flux measurements due to beam corrections, map calibrations and uncertainties in bandpasses are expected to be small, as discussed extensively in Planck Collaboration (2011d,c,e).

<sup>1</sup> *Planck* (<http://www.esa.int/planck>) is a project of the European Space Agency (ESA) with instruments provided by two scientific consortia funded by ESA member states (in particular the lead countries: France and Italy) with contributions from NASA (USA), and telescope reflectors provided in a collaboration between ESA and a scientific consortium led and funded by Denmark.

### 3. Reconstruction and analysis of the $y$ map

The Comptonization parameter  $y$  maps used in this work have been obtained using the MILCA (Modified Internal Linear Combination Algorithm) method (Hurier et al. 2010) on the *Planck* frequency maps from 100 GHz to 857 GHz in a region centered on the Coma cluster. MILCA is a component separation approach aimed at extracting a chosen component (in our case the thermal Sunyaev Zeldovich (tSZ) signal) from a multi-channel set of input maps. It is based mainly on the well known ILC approach (see for example Eriksen et al. 2004), which searches for the linear combination of the input maps that minimizes the variance of the final reconstructed map imposing spectral constraints. For this work, we apply MILCA using two constraints, the first to preserve the  $y$  signal and the second to remove CMB contamination in the final  $y$  map. Furthermore, we correct for the bias induced by the instrumental noise, and we simultaneously use the extra degrees of freedom (dof) to minimize residuals from other components (2 dof) and from the instrumental noise (2 dof). These would otherwise increase the variance of the final reconstructed  $y$  map. The noise covariance matrix is estimated from jack-knife maps. To improve the efficiency of the algorithm we perform our separation independently on several bins in the spatial-frequency plane. The final  $y$  map has an effective point spread function (PSF) with a resolution of 10' FWHM. Finally, to characterize the noise properties, such as correlation and inhomogeneities, we use jack-knife and redundancy maps for each frequency and apply the same linear transformation as used to compute the MILCA  $y$  map. The MILCA procedure provides us with a data map  $y(k, m)$  (where  $k$  and  $m$  are the abscissa and ordinate, respectively) together with random realisations of an additive noise model  $dy(k, m)$ , which is Gaussian, correlated, and may present some non-stationary behavior across the field of view. These maps are used to derive radial profiles and to perform the image analysis as described below.

We verified that the reconstruction methods GMCA (Bobin et al. 2008) and NILC (Remazeilles et al. 2011) give results that are consistent within the errors with the MILCA method (see Planck Collaboration V 2012).

#### 3.1. Analysis of radial profiles

In this paper, we present various radial profiles  $y(r)$  of the 2D distribution of the Comptonisation parameter  $y(k, m)$ . These allow us to study the underlying pressure distribution of the intracluster medium of Coma. The  $y$  parameter is proportional to the gas pressure  $P = n_e k T$  integrated along the line of sight:

$$y = \frac{\sigma_T}{m_e c^2} \int P(l) dl, \quad (1)$$

where  $n_e$  and  $T$  are the gas electron density and temperature,  $\sigma_T$  is the Thomson cross-section,  $k$  the Boltzmann constant,  $m_e$  the mass of the electron and  $c$  the speed of light. All the radial profiles  $y(r)$  are extracted from the  $y(k, m)$  map after masking out bright radio sources. In this work we model the observed  $y(r)$  projected profiles using the forward approach described in detail by e.g. Bourdin & Mazzotta (2008). We assume that the three-dimensional pressure profiles can be adequately represented by some analytic functions that have the freedom to describe a wide range of the possible profiles. The 3D model is projected along the line of sight assuming spherical symmetry and convolved with the *Planck* PSF to produce a projected model function

$f(r)$ . Finally we fit  $f(r)$  to the data using a chi-square minimisation of its distance from the radial profiles  $y(r) + dy(r)$  derived from the MILCA map including its additive noise model  $y(k, m) + dy(k, m)$ . This procedure allows us to decorrelate the additive noise fluctuations by projecting  $y(r)$  and the model  $f(r)$  onto the principal component basis of all realisations of the noise model, i.e. by diagonalizing its covariance matrix.

The confidence intervals on each parameter are calculated using the percentile method; i.e., we rank the fitted values and select the value corresponding to the chosen percentile. Suppose we have 1000 realizations for a specific parameter  $\zeta$  which is already ranked from bottom to top, the percentile confidence interval at 68% corresponds to  $[\zeta_{160^{th}}, \zeta_{840^{th}}]$ . Notice that in this work the confidence intervals are reported with respect to the best fit value obtained by fitting the model to the initial data set.

Note that, by design, the forward approach tests the capability of a specific functional to globally reproduce the observed data. For this reason, the error estimates represent the uncertainties on the parameters of the fitting function rather than the local uncertainties of the deprojected quantity. This technique has been fully tested on hydrodynamic simulations (e.g. Nagai et al. 2007; Meneghetti et al. 2010).

#### 3.2. Zero level of the $y$ map and the maximum detection radius

As a result of the extraction algorithm, *Planck*  $y$  maps are undetermined to an arbitrary additive constant  $y_{\text{off}}$ . This constant is a free parameter in all our  $y$ -map models. This constant can be determined from the *Planck* patch by measuring the  $y$  value at very large radii where we expect to have small or no contribution to the signal from the Cluster itself. In particular, in the case of the  $13.6^\circ \times 13.6^\circ$  MILCA-based patch of the image centered on Coma, this constant is negative, as illustrated in Fig. 1. The radial profile of  $y$  was extracted from the  $y$  map in a set of circular annuli centered at  $(\text{RA}_{\text{J2000}}, \text{DEC}_{\text{J2000}}) = (12:59:47, +27:55:53)$ . The errors assigned to the points are crudely estimated by calculating the variance of the  $y$  map blocked to a pixel size much larger than the size of the *Planck* PSF. The variance is then rescaled for each annulus, assuming that the correlation of the noise can be neglected on these spatial scales. For a model consisting of a power-law plus a constant (over the radial range from 85 arcmin to 300 arcmin) we find  $y_{\text{off}} = -6.3 \cdot 10^{-7} \pm 0.9 \cdot 10^{-7}$ . We note that the precise value of  $y_{\text{off}}$  depends weakly on the particular model used, and on the range of radii involved in the fitting.

To determine the maximum radius at which *Planck* detects a significant excess of  $y$  compared to the rest of the image, we adopted the following procedure. For every annulus around Coma with measured  $y = y_{\text{Coma}}$  we have calculated the distribution of  $y = y_{\text{random}}$  measured in  $N = 300$  annuli of a similar size, but with the centers randomly placed in any part of the image outside the  $5 \times R_{500}$  circle around Coma, where  $R_{500}$  is the radius at which the cluster density contrast is  $\Delta = 500$ . When calculating  $y_{\text{random}}$  the parts of the annuli within  $5 \times R_{500}$  were excluded. The comparison of  $y_{\text{Coma}}$  with the distribution of  $y_{\text{random}}$  is used to conservatively estimate the probability of getting  $y > y_{\text{Coma}}$  by chance in an annulus of a given size at a random position in the image (see Fig. 1, lower panel). For the annulus between 2.6 and 3.1  $R_{500}$  (122 arcmin to 147 arcmin) the probability of getting  $y_{\text{Coma}}$  by chance is  $\approx 3 \cdot 10^{-3}$  (a crude estimate, given  $N = 300$  random positions). For smaller radii the probability is much lower, while at larger radii the probability of getting  $y$  in excess of  $y_{\text{Coma}}$  is  $\sim 10\%$  or higher. We conclude that *Planck*

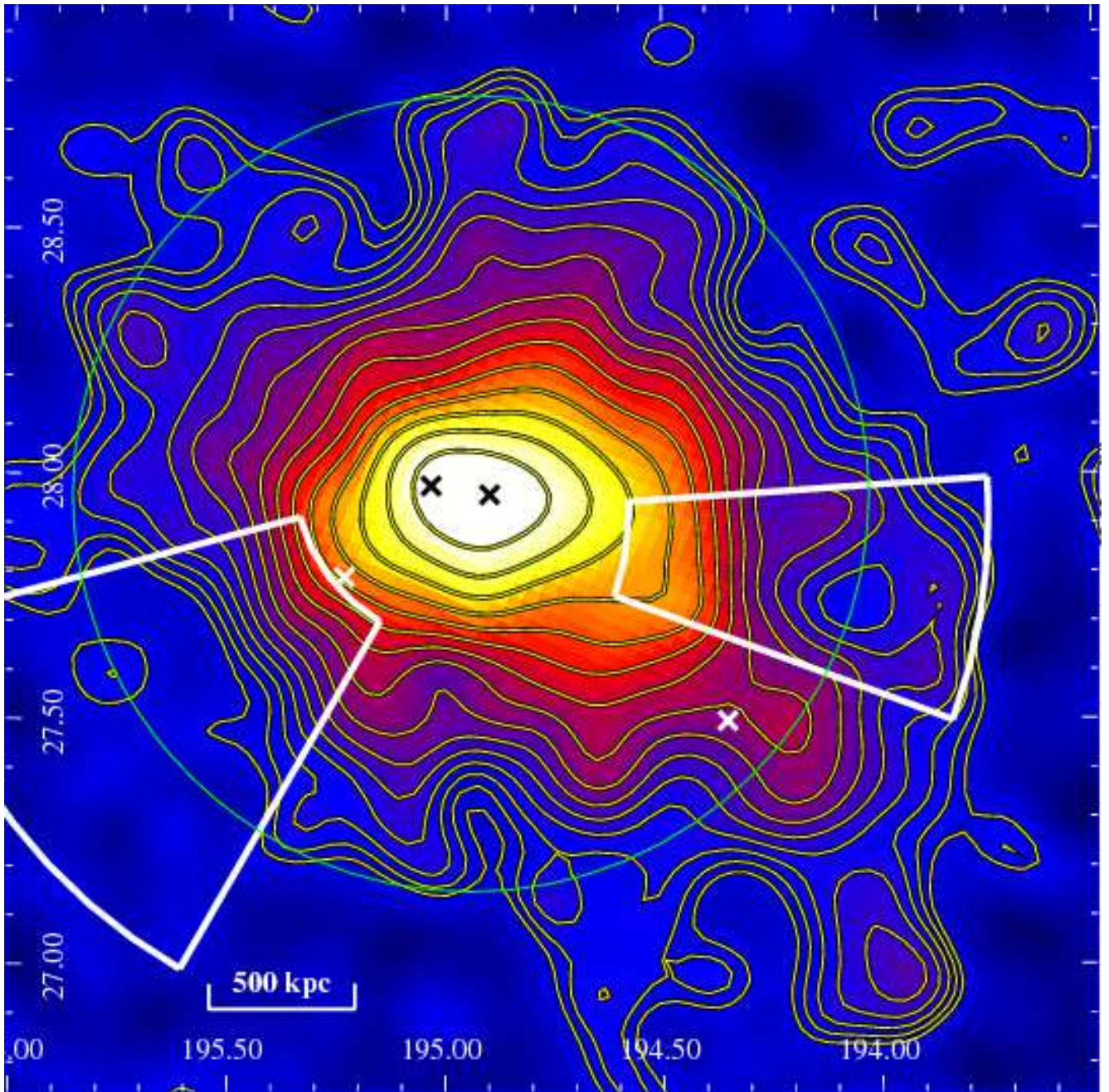


Fig. 2: The *Planck*  $y$  map of the Coma cluster obtained combining the HFI channels from 100 GHz to 857 GHz. North is up and west is to the right. The map is corrected for the additive constant  $y_{\text{off}}$ . The final map bin corresponds to  $\text{FWHM} = 10'$ . The image is about  $130 \times 130$  arcminutes $^2$ . The contour levels are logarithmically spaced by  $\sqrt[4]{2}$  (every 4 lines,  $y$  increases by a factor 2). The outermost contour corresponds to  $y = 2 \times \sigma_{\text{noise}} = 4.6 \times 10^{-6}$ . The green circle indicates  $R_{500}$ . White and black crosses indicate the position of the brightest galaxies in Coma. The white sectors indicate two regions where the  $y$  map shows a local steepening of the radial gradient (see Section 7 and Fig. 6).

detects the signal from Coma in narrow annuli  $\Delta R/R = 0.2$  at least up to  $R_{\text{max}} \sim 3 \times R_{500}$ . This is a conservative and model-independent estimate. In the rest of the paper we use parametric models which cover the full range of radii to fully exploit *Planck* data even beyond  $R_{\text{max}}$ .

#### 4. XMM-Newton data analysis

The *XMM-Newton* results presented in this paper have been derived from analysis of the mosaic obtained combining 27 *XMM-*

*Newton* pointings of the Coma cluster available in the archive. The *XMM-Newton* data have been prepared and analyzed using the procedure described in detail in [Bourdin et al. \(2011\)](#), and [Bourdin & Mazzotta \(2008\)](#). We estimated the  $Y_X = M_{\text{gas}} \times T$  parameter of Coma iteratively using the  $Y_X - M_{500}$  scaling relation calibrated from hydrostatic mass estimates in a nearby cluster sample observed with *XMM-Newton* ([Arnaud et al. 2010](#)); we find  $R_{500} \approx (47 \pm 1)\text{arcmin} \approx (1.31 \pm 0.03)\text{Mpc}$  and we use this value throughout the paper. To study the surface brightness and temperature radial profiles we use the forward approach

described in [Bourdin et al. \(2011\)](#) taking care to project the temperature profile using the formula appropriate for spectroscopy; i.e., we use the spectroscopic-like temperature introduced by [Mazzotta et al. 2004](#).

## 5. The Coma $y$ maps

The main goal of this paper is to present the radial and sectoral properties of the SZ signal from the Coma cluster. Here we describe some general properties of the image; the full image analysis will be presented in a forthcoming paper that will make use of all the *Planck* data, including the extended surveys.

Fig. 2 shows the *Planck*  $y$  map of the Coma cluster obtained by combining the HFI channels from 100 GHz to 857 GHz. The effective point spread function (PSF) of this map corresponds to  $\text{FWHM} = 10'$  and its noise level is  $\sigma_{\text{noise}10} = 2.3 \times 10^{-6}$ .

To highlight the spatial structure of the  $y$  map, in Fig. 2 we overlay the contour levels of the  $y$  signal. We notice that at this resolution, the  $y$  signal observed by *Planck* traces the pressure distribution of the ICM up to  $R_{500}$ . As is already known from X-ray observations (e.g. [Briel et al. 1992](#); [White et al. 1993](#); [Neumann et al. 2003](#)), the *Planck*  $y$  map shows that the gas in Coma is elongated towards the west and extends in the southwest direction toward the NGC4839 subgroup. Fig. 2 shows that the SZ signal from this subgroup is clearly detected by *Planck* (see the white cross to the southwest).

The *Planck*  $y$  map of the Coma cluster also shows at least two marked local steepenings of the radial gradient, to the west and to the southeast with respect to the cluster center. For convenience, in Fig. 2 we outline these regions with white sectors. A steepening of the  $y$  radial gradient suggests the presence of a discontinuity in the cluster pressure profile which may be produced by a thermal shock, as we discuss in Section 7. In Fig. 3 we show the *Planck*  $y$  map of the Coma cluster obtained by adding the 70 GHz channel of LFI to the HFI channels and smoothing to a lower resolution. The PSF of this map corresponds to  $\text{FWHM} = 30'$  which lowers the noise level by approximately one order of magnitude with respect to the  $10'$  resolution map:  $\sigma_{\text{noise}30} = 3.35 \times 10^{-7}$ . As for Fig. 2 the outermost contour level indicates  $y = 2 \times \sigma_{\text{noise}30} = 6.7 \times 10^{-7}$ . Due to the larger smoothing, this map shows less structure in the cluster center, but clearly highlights that *Planck* can easily trace the pressure profile of the ICM well beyond  $R_{200} \approx 2 \times R_{500}$  (see the outermost circle in Figure 3).

## 6. Azimuthally averaged profile

Before studying the azimuthally averaged SZ profile of the Coma cluster in detail, we first show a very simple performance test. In Fig. 4 we compare the SZ effect toward the Coma cluster, in units of the Rayleigh-Jeans equivalent temperature, measured by *Planck* and by *WMAP* using the optimal V and W bands (from Fig. 14 of [Komatsu et al. 2011](#)). This figure shows that, in addition to its greatly improved angular resolution, *Planck* frequency coverage results in errors on the profile which are  $\approx 20$  times smaller than those from *WMAP*. Thanks to this higher sensitivity *Planck* allows us to study, for the first time, the SZ signal of the Coma Cluster to its very outermost regions. We do this by extracting the  $y$  radial profile in concentric annuli centered on the cluster centroid (RA,Dec)=(12:59:47,+27:55:53).

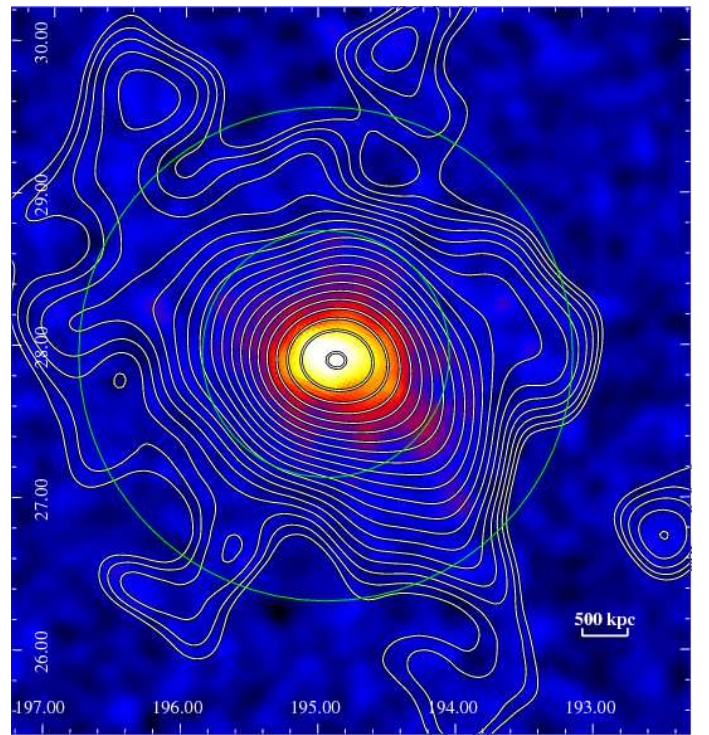


Fig. 3: The *Planck*  $y$  map of the Coma cluster obtained by combining the 70 GHz channel of LFI and the HFI channels from 100 GHz to 857 GHz. The map has been smoothed to have a PSF with  $\text{FWHM} = 30'$ . The image is about  $266 \times 266 \text{ arcmin}^2$ . The outermost contour corresponds to  $y = 2 \times \sigma_{\text{noise}30} = 6.7 \times 10^{-7}$ . The green circles indicate  $R_{500}$  and  $2 \times R_{500} \approx R_{200}$ .

We fit the observed  $y$  profile using the pressure formula proposed by [Arnaud et al. \(2010\)](#):

$$P(x) = \frac{P_0}{(c_{500}x)^\gamma [1 + (c_{500}x)^\alpha]^{(\beta-\gamma)/\alpha}}, \quad (2)$$

where,  $x = (R/R_{500})$ . This is done by fixing  $R_{500}$  at the best-fit value obtained from the X-ray analysis ( $R_{500} = 1.31 \text{ Mpc}$ , see section 4) and using three different combinations of parameters which we itemize below:

- a “universal” pressure model (which we will refer to as Model A) for which we leave only  $P_0$  as a free parameter and fix  $c_{500} = 1.177$ ,  $\gamma = 0.3081$ ,  $\alpha = 1.0510$ ,  $\beta = 5.4905$  ([Arnaud et al. 2010](#));
- a pressure profile appropriate for clusters with disturbed X-ray morphology (Model B) for which we leave  $P_0$  as a free parameter and fix  $c_{500} = 1.083$ ,  $\gamma = 0.3798$ ,  $\alpha = 1.406$ ,  $\beta = 5.4905$  ([Arnaud et al. 2010](#));
- a modified pressure profile (Model C) for which we let all the parameters vary (except  $R_{500}$ ).

The best-fit parameters, together with their 68% confidence level errors, are reported in Table 1 and the resulting best-fit models are overlaid in the upper left, upper right and lower left panels of Fig. 5, for models A, B, and C, respectively. We find that Eq. 2 fits the observed  $y$  profile only if all the parameters (except  $R_{500}$ ) are left free to vary (i.e., Model C).

We also fit the observed radial  $y$  profile using a fitting formula (Model D) derived from the density and temperature functionals introduced by [Vikhlinin et al. \(2006\)](#):

$$P = n_e \times kT \quad (3)$$

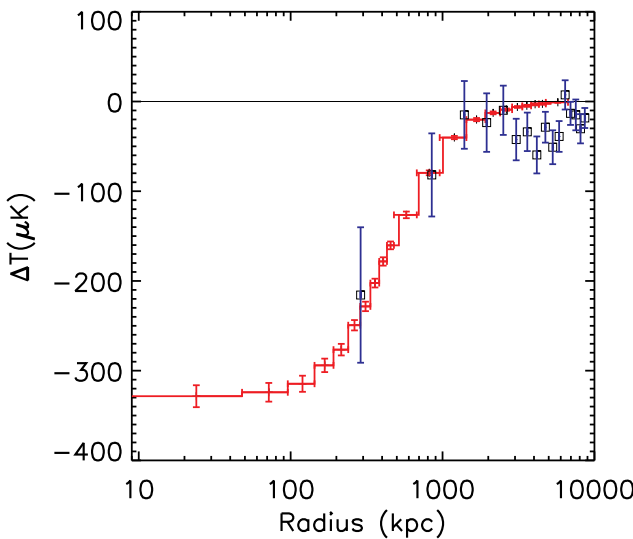


Fig. 4: Comparison of the radial profile of the SZ effect towards the Coma cluster, in units of the Rayleigh-Jeans equivalent temperature measured by *Planck* (crosses) with the one obtained by *WMAP* (open squares) using the optimal V and W band (from Fig. 14 of [Komatsu et al. 2011](#)). The plotted *Planck* errors are the square root of the diagonal elements of the covariance matrix. Notice that profiles have been extracted from SZ maps with 10' and 30' angular resolution from *Planck* and *WMAP*, respectively.

where,

$$n_e^2(r) = n_0^2 \frac{(r/r_c)^{-\alpha}}{[1 + (r/r_c)^2]^{3\beta-\alpha/2}} \frac{1}{[1 + (r/r_s)^3]^{\epsilon/3}} + \frac{n_{02}^2}{[1 + (r/r_{c2})^2]^{3\beta_2}}, \quad (4)$$

and

$$T(r) = T_o \frac{(r/r_t)^{-\alpha}}{[1 + (r/r_t)^b]^{c/b}}. \quad (5)$$

The best fit parameters, together with their 68% confidence level errors, are reported in Table 2. The resulting model is overlaid in the lower-right panel of Fig. 5. The above temperature and density functions contain many more free parameters than Eq. (2). All these parameters have been specifically introduced to adequately fit all the observed surface brightness and temperature profiles of X-ray clusters of galaxies. This function thus is capable, in principle, of providing a better fit to any observed SZ profile. Despite this, we find that compared with Model C, Model D does not significantly improve the quality of the fit.

## 7. Pressure jumps

Fig. 2 shows that Coma exhibits a marked local steepening of the radial gradient of its  $y$  signal at about 0.5 degrees to the west and a similar distance to the southeast of the cluster centre. This suggests the presence of discontinuities in the underlying cluster pressure profiles. To test this hypothesis and to try to estimate the amplitude and the position of the pressure jumps we use the following simplified approach: i) we select two sectors ii) we extract the  $y$  profiles using circular annuli and iii) assuming spherical symmetry, we fit them to a 3D pressure model with a pressure

jump. The sectors are selected in order to follow, as closely as possible, the curvature of the  $y$  signal around the possible pressure jumps. This procedure is a bit arbitrary: the pressure jumps are not perfectly spherical symmetric, thus, the sector selection depends also on what is initially thought to be the leading edge of the underlying pressure jump. Choosing a sector that does not properly sample the pressure jump goes in the direction of mixing the signal from the pre and post pressure jump regions. The result is a smoother profile which, when fitted with the 3D pressure model, returns a smaller amplitude for the pressure jump itself. Thus, in the worst scenario, the measured pressure jumps represent a lower estimate of the jumps at the leading edges. In this work we set the centers and orientations of the west and the southeast sectors to the values reported in the first three columns of Table 3 and indicated in Fig. 2. In section 9.3 below we show that, within the selected sectors, the SZ and the X-ray analyses give consistent results. This indicates that i) these SZ-selected sectors are representative of the features under study and ii) that the hypothesis of spherical symmetry is a good approximation, at least within the selected sectors.

We fit the profiles using a 3D pressure model composed of two power-laws with index  $\eta_1$  and  $\eta_2$  and a jump by a factor  $D_J$  at the radius  $r_J$ . It is important to note that, even if irrelevant for the estimate of the jump amplitude, the measure of both the slope  $\eta_2$  and the absolute normalization of the 3D pressure at a given radius depends on the slope and extension of the ICM along the line of sight. To take this into account we assume that outside the fitting region (i.e. at  $r > r_s$ , with  $r_s = 2\text{Mpc}$ ) the slope of the pressure profile follows the asymptotic average pressure profile corresponding to model C (i.e.  $\eta_3 = \beta = 3.66$ ; see section 6 and Table 1). The 3D pressure profile is thus given by:

$$P = P_0 \times \begin{cases} D_J(r/r_J)^{-\eta_1} & r < r_J \\ (r/r_J)^{-\eta_2} & r_J < r < r_s \\ (r_s/r_J)^{-\eta_2} (r/r_s)^{-\eta_3} & r > r_s \end{cases} \quad (6)$$

We project the above 3D pressure model integrating along the line of sight for  $r < 10\text{Mpc}$ .

The best fit parameters together with their 68% errors are reported in Table 3. Note, that the error bars on  $r_J$  are smaller than the angular resolution of *Planck*. As explained in the Appendix A, this is not surprising and is simply due to projection effects.

In the left and right panels of Fig. 7 we show with a gray shadow the corresponding 3D pressure jump models with their errors for the west and southeast sectors, respectively. For convenience in Fig. 6 we overlay the data points with the best fit projected  $y$  models and we show the ratio between the observed and the best fit model of the projected  $y$  profile in units of the relative error. This figure clearly shows that the pressure jump model provides a good fit to the observed profiles for both the west and southeast sectors.

As reported in Table 3 the pressure jumps corresponding to the observed profiles are  $D_J = 4.5^{+2.50}_{-0.08}$  and  $D_J = 4.9^{+0.7}_{-0.2}$  for the west and southeast sectors, respectively.

## 8. SZ-Radio comparison

In Fig. 8 we overlay the  $y$  contour levels from Fig. 2 with the 352 MHz Westerbork Synthesis Radio Telescope diffuse total intensity image of the Coma cluster from Fig. 3 of [Brown & Rudnick \(2011\)](#). Most of the emission from compact radio sources both in and behind the cluster has been automatically subtracted. This image clearly shows a correlation between the diffuse radio emission and the  $y$  signal.

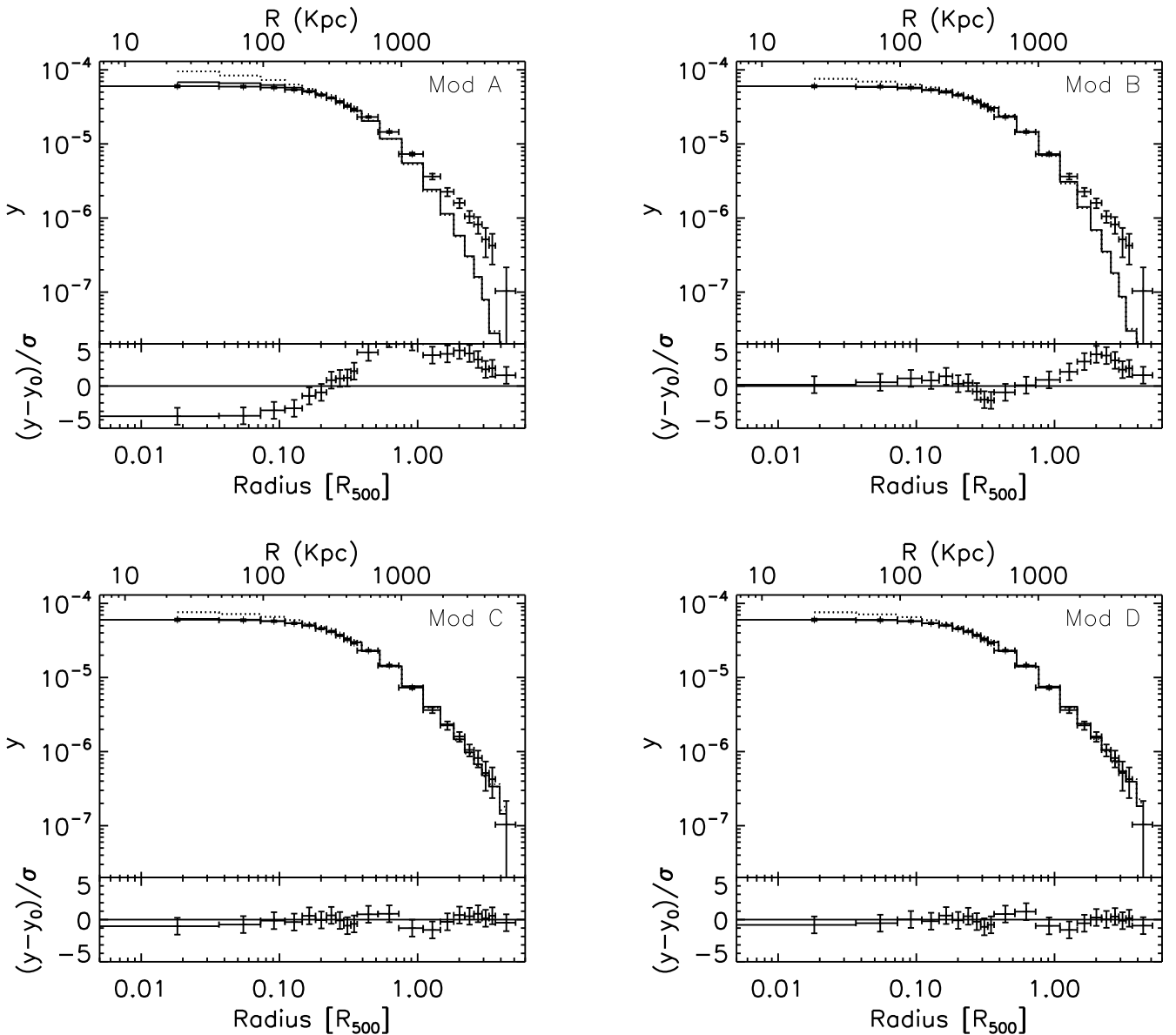


Fig. 5: Comparison between the azimuthally averaged  $y$  profile of the Coma cluster and various models. From left to right, top to bottom, we show the best-fit  $y$  models corresponding to the Arnaud et al. “universal” profile (A), the “universal” profile for merger systems (B), the modified “universal” profile (C, see 1), and the Vikhlinin et al. fitting formula (D, see 2). For each panel we show in the *Upper subpanel* points indicating the Coma  $y$  profile extracted in circular annuli centered at  $(RA_{J2000}, DEC_{J2000}) = (12:59:47, +27:55:53)$ . The plotted errors are the square root of the diagonal elements of the covariance matrix. Continuous and dotted histograms are the best fit projected  $y$  model after and before the convolution with the *Planck* PSF, respectively. In the *Lower subpanel* we show the ratio between the observed and the best fit model of the projected  $y$  profile in units of the relative error.

To provide a more quantitative comparison of the observed correlation, we convolve the the diffuse radio emission to 10 arcmin resolution to match the *Planck*  $y$  map. We then extract the radio and  $y$  signals from the innermost  $r < 50$  arcmin region of the cluster and plot the results in Fig. 9. This is the first quantitative surface-brightness comparison of radio and SZ brightnesses<sup>2</sup>. We fit the data in the log-log plane using the Bayesian linear regression algorithm proposed by Kelly (2007) which ac-

counts for errors in both X and Y. We find a quasi-linear relation between the radio emission and the  $y$  signal:

$$\frac{y}{10^{-5}} = 10^{(0.86 \pm 0.02)} F_R^{(0.92 \pm 0.04)}, \quad (7)$$

where  $F_R$  is the radio brightness in Jy/beam (10 arcmin beam FWHM).

Furthermore, using the same algorithm, we find that the intrinsic scatter between the two observables is only  $\sigma_{\text{scatter}} = (9.6 \pm 0.2)\%$ . The quasi-linear relation between the radio emission and  $y$  signal, and its small scatter, are also clear from the good match of the radio and  $y$  profiles shown in Fig. 10 obtained

<sup>2</sup> see Malu & Subrahmanyam (2012) for a morphological comparison between radio and SZ brightnesses in the Bullet cluster

Table 1: Best Fit Parameters for the [Arnaud et al. \(2010\)](#) pressure model (Eq. 4 and Eq. 5)

model (Mpc)	$P_0$ ( $10^{-2}$ )	$c_{500}$	$\gamma$	$\alpha$	$\beta$	$R_{500}$ (Mpc)
A (“Universal”)	$2.23^{+0.03}_{-0.04}$	1.17	0.308	1.051	5.4905	1.31
B (“Universal” merger)	$0.98^{+0.02}_{-0.02}$	1.083	0.3798	1.406	5.49	1.31
C (“Universal” all free)	$3.51^{+0.05}_{-0.17}$	$2.35^{+0.12}_{-0.01}$	< 0.01	$1.21^{+0.06}_{-0.02}$	$3.66^{+0.50}_{-0.08}$	1.31

Table 2: Best Fit Parameters for Model D pressure model ([Vikhlinin et al. 2006](#)) (eq. 3)

Density		Temperature	
$n_0(10^{-3}\text{cm}^{-3})$	$4.6^{+0.1}_{-0.1}$	$T_0(\text{KeV})$	$9.2^{+0.2}_{-0.3}$
$r_c(\text{Mpc})$	$0.18^{+0.02}_{-0.01}$	$r_t(\text{Mpc})$	$1.15^{+0.1}_{-0.1}$
$r_s(\text{Mpc})$	$0.78^{+0.03}_{-0.03}$	$a$	$-0.20^{+0.01}_{-0.02}$
$\alpha$	$0.12^{+0.02}_{-0.01}$	$b$	$0.9^{+2.0}_{-0.2}$
$\beta$	$0.59^{+0.02}_{-0.02}$	$c$	$0.0^{+0.04}_{-0.00}$
$\gamma$	3		
$\epsilon$	$3.02^{+0.12}_{-0.15}$		
$n_{02}(\text{cm}^{-3})$	$0^a$		

<sup>a</sup> The fit returns  $n_{02} = 0$  thus  $r_{c2}$  and  $\beta_2$  are arbitrary.

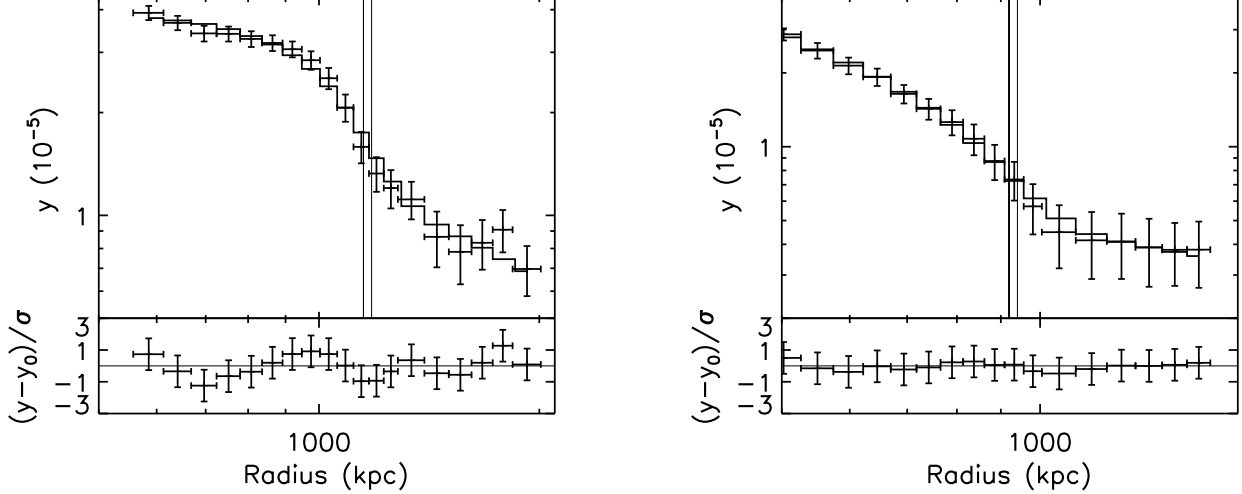


Fig. 6: Comparison between the projected  $y$  radial profile and the best fit  $y$  shock model of the west (left) and southeast (right) pressure jumps. *Upper panel*: The points indicate the Coma  $y$  profile extracted from the respective sectors whose centers and position angles are reported in table 3. The plotted errors are the square root of the diagonal elements of the covariance matrix. The continuous histogram is the best fit projected  $y$  model reported in Table 3. The two vertical lines mark the  $\pm 1\sigma$  position range of the jump. *Lower panel*: Ratio between the observed and the best fit model of the projected  $y$  profile in units of the relative error.

by simply rescaling the  $10'$  FWHM convolved radio profile by  $10^{0.86} \times 10^5$ . An approximate linear relationship between the radio halo and SZ total powers for a sample of clusters was also found by [Basu \(2012\)](#), for the case that the signals are calculated over the volume of the radio halos.

## 9. Discussion

So far In this paper we have presented the data analysis of the Coma cluster observed in its SZ effect by the *Planck* satellite. In Section 5 and Section 6 we showed that, thanks to its great sensitivity, *Planck* is capable of detecting significant SZ emis-

sion above the zero level of the  $y$  map up to at least 4 Mpc which corresponds to  $R \approx 3 \times R_{500}$ . This allows, for the first time, the study of the ICM pressure distribution in the outermost cluster regions. Furthermore, we performed a comparison with radio synchrotron signals. Here we discuss our results in more detail.

### 9.1. Global pressure profile

To study the 3D pressure distribution of the ICM up to  $r = 3 - 4 \times R_{500}$ , we fit the observed  $y$  profile using four analytic models summarized in Table 1 and Table 2 (see Section 6).

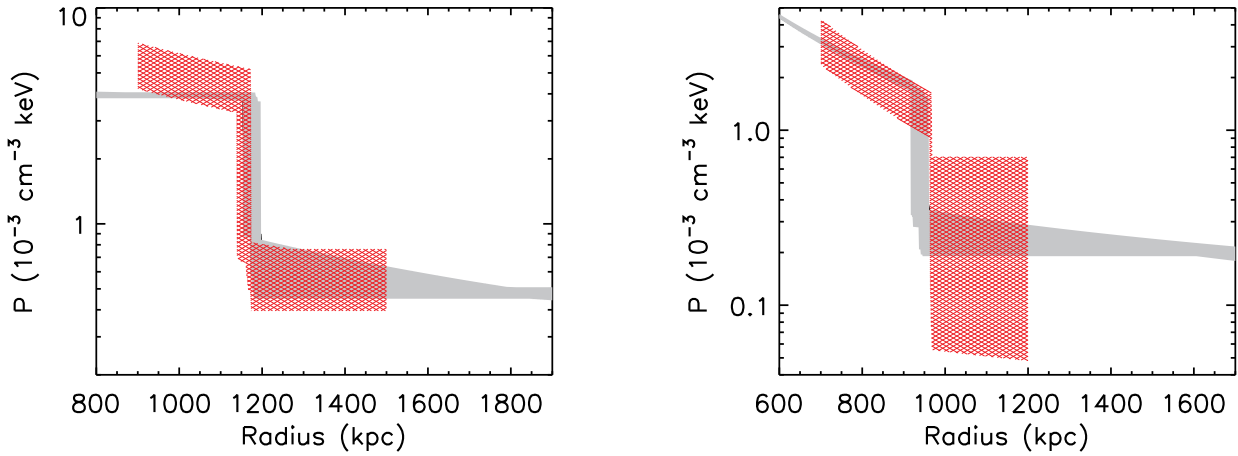


Fig. 7: 68% confidence level range of the 3D-pressure model for the west (left panel) and southeast (right panel) sectors in Fig. 6. Gray shadows are the profiles derived from the *Planck* data. Red shadows are the profiles derived from the *XMM-Newton* data.

Table 3: Best-fit parameters of the pressure jump model of Eq. (6)

Sector	<sup>a</sup> RA (J2000)	<sup>a</sup> Dec (J2000)	<sup>a</sup> Position angle (deg:deg)	$P_0$ ( $10^{-4}$ cm $^{-3}$ keV)	$r_J$ (Mpc)	$D_J$	$\eta_1$	$\eta_2$
West	13:00:25.6	+27:54:44.00	340:364	$8.8^{+0.1}_{-0.1}$	$1.15^{+0.03}_{-0.00}$	$4.5^{+2.5}_{-0.1}$	$0.0^{+0.20}_{-0.00}$	$1.28^{+0.02}_{-1.28}$
Southeast	12:59:48.9	+28:00:14.39	195:240	$3.6^{+0.7}_{-0.5}$	$0.92^{+0.02}_{-0.00}$	$4.9^{+0.7}_{-0.2}$	$2.1^{+0.09}_{-0.02}$	$1.00^{+0.06}_{-0.30}$

<sup>a</sup> The RA and Dec indicate the center of curvature of the sectors from which the profiles have been extracted.

<sup>b</sup> We fixed  $r_s = 2$  Mpc and  $\eta_3 = 3.66$  (see text).

From the ratio plot shown in Fig. 5 we immediately see that the “universal” pressure profile (Model A) is too steep both in the cluster center and in the outskirts. The fit to the data thus results in an overestimation and underestimation of the observed SZ signal at smaller and larger radii, respectively. The overestimation of the observed profile at lower radii is consistent with *WMAP* (Komatsu et al. 2011). This is expected since merging systems, such as Coma, have a flatter central pressure profile than the “universal” model (Arnaud et al. 2010). For merging systems, Model B should provide a better fit as it has been specifically calibrated, at  $r < R_{500}$ , to reproduce the average X-ray profiles of such systems (Arnaud et al. 2010). Fig. 5 shows that this latter model indeed reproduces the data well at  $r < R_{500}$ . Nevertheless, as for Model A, it still underestimates the observed y signal at larger radii. The observed profile clearly requires a shallower pressure profile in the cluster outskirts as evident in Models C and D. This is important as the external pressure slopes of both Model A and B are tuned to reproduce the mean slope predicted by the hydrodynamic simulations of Borgani et al. (2004); Nagai et al. (2007); Piffaretti & Valdarnini (2008) (from now on, B04+N07+P08). The *Planck* observation shows that the pressure slope for Coma is flatter than this value. This is also illustrated in Fig. 11 where we report the pressure slope as a function of the radius in our models: we find that while at  $R = 3 \times R_{500}$  the mean predicted pressure slope is  $> 4.5$  for Models A and B, the observed pressure slope of Coma is  $\approx 3.5$  as seen in Model C and Model D. In Fig. 12 we compare the scaled pressure profile of Coma with the pressure profiles derived from the B04+N07+P08 numerical simulations. We find that the Coma

pressure profile at  $2 \times R_{500}$  is already 2 times higher than the average profile predicted by these hydrodynamics simulations although still within the overall profile distribution which has a quite large scatter. The Coma pressure profile thus lies on the upper envelope of the pressure profile distribution derived from the above simulations. Note that the recent numerical simulations of Battaglia et al. (2011) predict a flatter mean pressure profile which appears to be more consistent with the Coma profile and, in general, with the *Planck* SZ pressure profile obtained by stacking 62 nearby massive clusters (Planck Collaboration V 2012). It is beyond the scope of this paper to discuss in detail the comparison between theoretical predictions. Here we just stress that, at such large radii, there is the possibility that the observed SZ signal could be significantly contaminated by SZ sources along the line of sight. This signal could be generated by i) unresolved and undetected clusters and ii) hot-warm gas filaments. Contamination would produce an apparent flattening of the pressure profile. We tested for possible contamination by unresolved clusters by re-extracting the y profile excluding circular regions of  $r = 5'$  centered on all NED identified clusters of galaxies present in the Coma cluster region. We find that the new y profile is consistent within the errors with the previous one, which implies that this kind of contamination is negligible in the Coma region. Thus, if there is SZ contamination it is probably related to the filamentary structures surrounding the cluster. We note that from the re-analysis of the *ROSAT* All-Sky Survey, Bonamente et al. (2009) and Bonamente et al. (2003) report the detection of extended soft X-ray emission in the Coma cluster region up to 5 Mpc from the cluster center. They propose that this

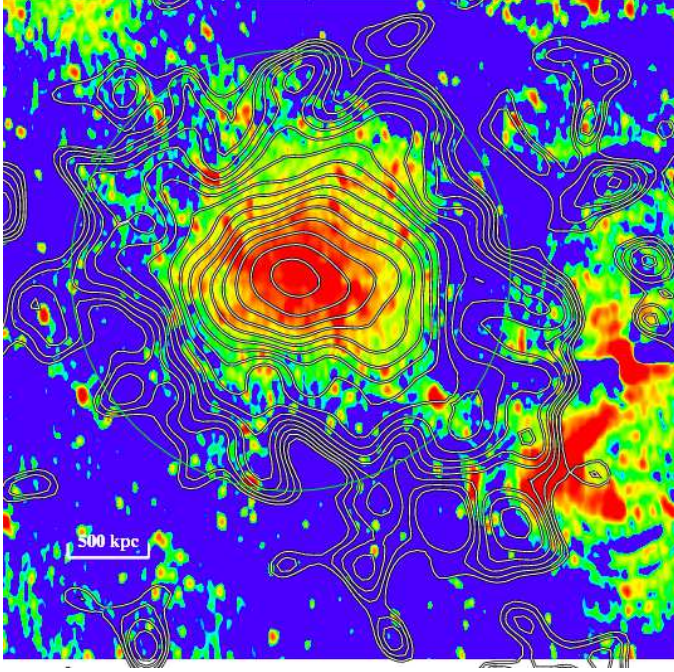


Fig. 8: Westerbork Synthesis Radio Telescope 352 MHz total intensity image of the Coma Cluster from Figure 3 of [Brown & Rudnick \(2011\)](#) overlaid by the  $y$  contour levels from Fig. 2. Most of the radio flux from compact sources has been subtracted; the resolution is 133 arcsec  $\times$  68 arcsec at -1.5 degrees (W of N). The green circle indicates  $R_{500}$ .

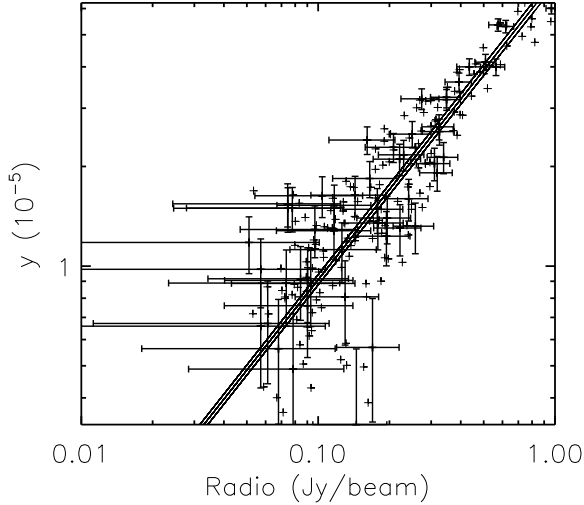


Fig. 9: Scatter plot between the radio map after smoothing to  $\text{FWHM} = 10'$  and the  $y$  signal for the Coma cluster. To make the plot clearer, we show errors only for some points.

emission is related to filaments that converge toward Coma and is generated either by nonthermal radiation caused by accretion shocks or by thermal emission from the filaments themselves.

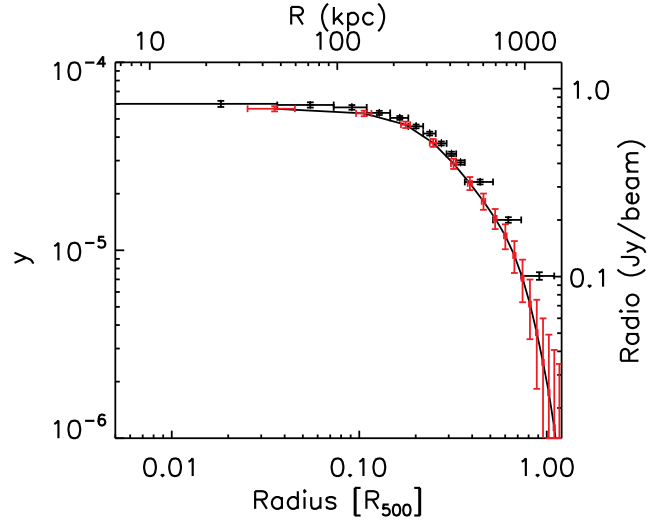


Fig. 10: Comparison of the  $y$  (black) and diffuse radio (red) global radio profiles in Coma. The radio profile has been convolved to 10 arcmin resolution to match the *Planck* FWHM and simply rescaled by the multiplication factor derived from the linear regression shown in Fig. 9. The radio errors are dominated by uncertainties in the zero level due to a weak bowl resulting from the lack of short interferometer spacings.

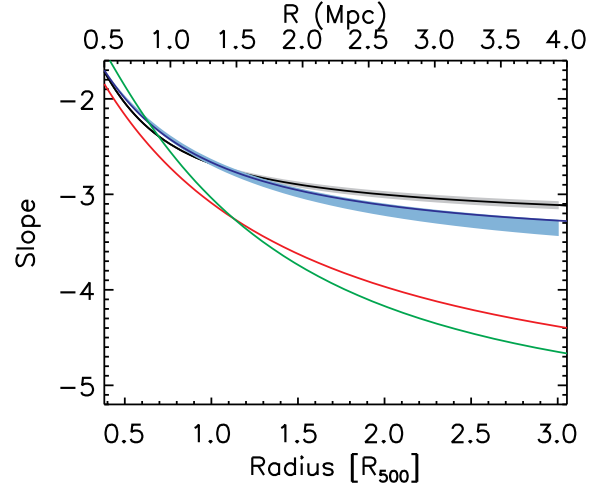


Fig. 11: Comparison of the pressure slopes of the best-fit models shown in Fig. 5. The red, green, blue and grey lines correspond to Models A, B, C, and D, respectively.

## 9.2. X-ray and SZ pressure profile comparison

We can compare the 3D pressure profile derived from the SZ observations to those obtained by multiplying the 3D electron density and the gas temperature profiles derived from the data analysis of the *XMM-Newton* mosaic of Coma

In Fig. 13 we compare the 3D X-ray pressure profile with the 3D SZ profile of our reference Model C. We point the reader's attention to the very large dynamical range shown in the figure: the radius extends up to  $r = 4$  Mpc probing approximately four

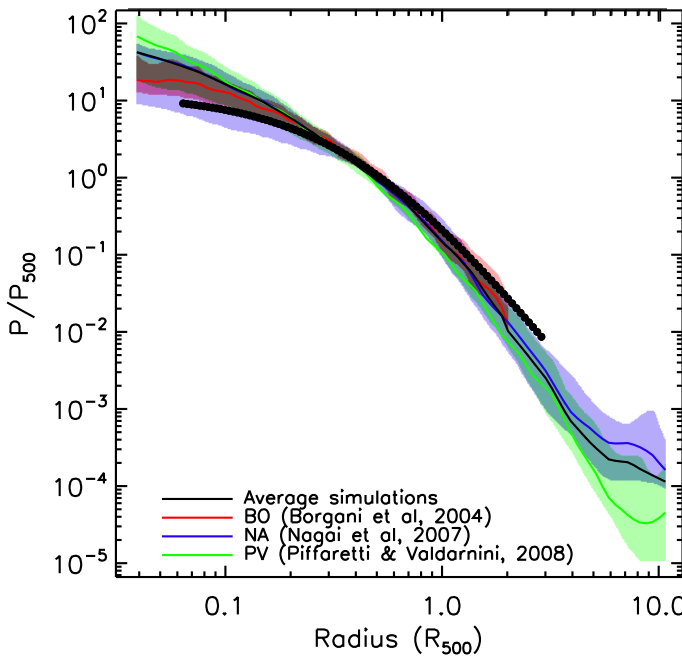


Fig. 12: Scaled Coma pressure profile with relative errors (black shadow) overplotted on the scaled pressure profiles derived from numerical simulations from Fig. 6 of Arnaud et al. (2010).

orders of magnitude in pressure. In contrast, due to a combination of i) relatively high background levels and ii) the available mosaic observations, *XMM-Newton* can probe the ICM pressure profile of Coma only up to  $\approx 1$  Mpc i.e., four times smaller radii than *Planck*, probing only  $\approx$  one order of magnitude in pressure.

Due to the good statistics of both *Planck* and *XMM-Newton* data, we see that the pressure profile derived from *Planck* appears significantly lower than that of *XMM-Newton*, even if they differ by only 10-15%. This low, but significant, discrepancy may be related to the fact that we are applying spherical models to a cluster that has a much more complex morphology, with a number of substructures. A detailed structure analysis exploring these apparent pressure profile discrepancies is beyond the scope of this paper and will be presented in a forthcoming paper. Here we just show a comparison of the 3D pressure profiles obtained from *Planck* and *XMM-Newton* in four  $90^\circ$  sectors centered on the cluster and oriented towards the four cardinal points (see Fig. 14). This shows that the pressure discrepancy depends strongly on the sector considered. In particular, we find that while in the north sector the *Planck* and *XMM-Newton* pressure profiles agree within the errors, in the west sector we find the largest discrepancy, up to 25-30%. As known from X-ray observations (see e.g., Neumann et al. 2003) the north sector is the one that is more regular, while the west sector is the one in which the ICM is strongly elongated with the presence of major structures.

### 9.3. Shocks

In Section 7 we show that Coma exhibits a localized steepening of its  $y$  profile in at least two directions, to the west and to the southeast. These suggest the presence of discontinuities in the underlying 3D pressure profile of the cluster. Using two sectors designed to follow the curvature of the  $y$  signal around the

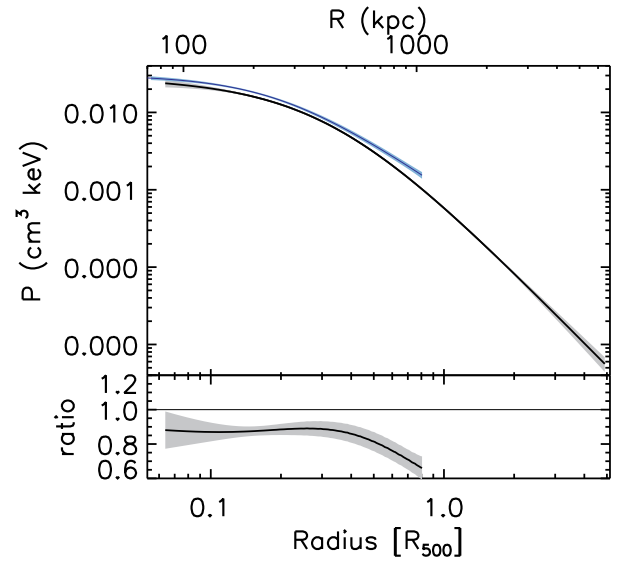


Fig. 13: Comparison between the *Planck* and *XMM-Newton*-derived deprojected total pressure profiles. *Upper panel*: Blue line and light blue shadow: deprojected pressure profile, with its 68% confidence level errors, obtained from the X-ray analysis of the *XMM-Newton* data (see text). Black line and gray shadow: best fit and 68% confidence level errors from the Model C pressure profile resulting from the fit shown in Fig. 5. *Lower panel*: Ratio between the *XMM-Newton* and *Planck*-derived pressure profiles. The black line and the gray shadow indicate the best fit and the 68% confidence level errors, respectively.

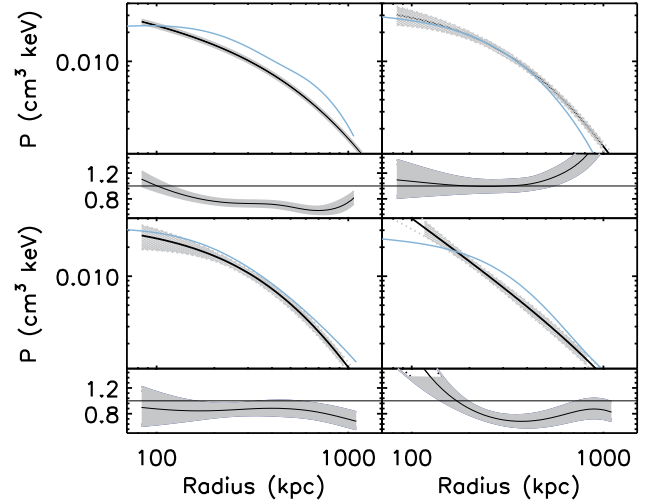


Fig. 14: Same as Fig. 13 but from profiles extracted in 4  $90^\circ$  sectors. From left to right, top to bottom we report the west ( $-45^\circ, 45^\circ$ ), north ( $45^\circ, 135^\circ$ ), east ( $135^\circ, 225^\circ$ ) and south ( $225^\circ, 3155^\circ$ ) sectors, respectively.

pressure jumps we estimate their amplitudes. This represents the first attempt to identify and estimate the amplitude of possible pressure jumps in the cluster atmosphere directly from the SZ signal. Interestingly, we find that similar features are observed at the same locations in the X-ray and radio bands.

In Fig. 15 we compare the X-ray and radio cluster properties from the west and southeast sectors selected from the SZ image.

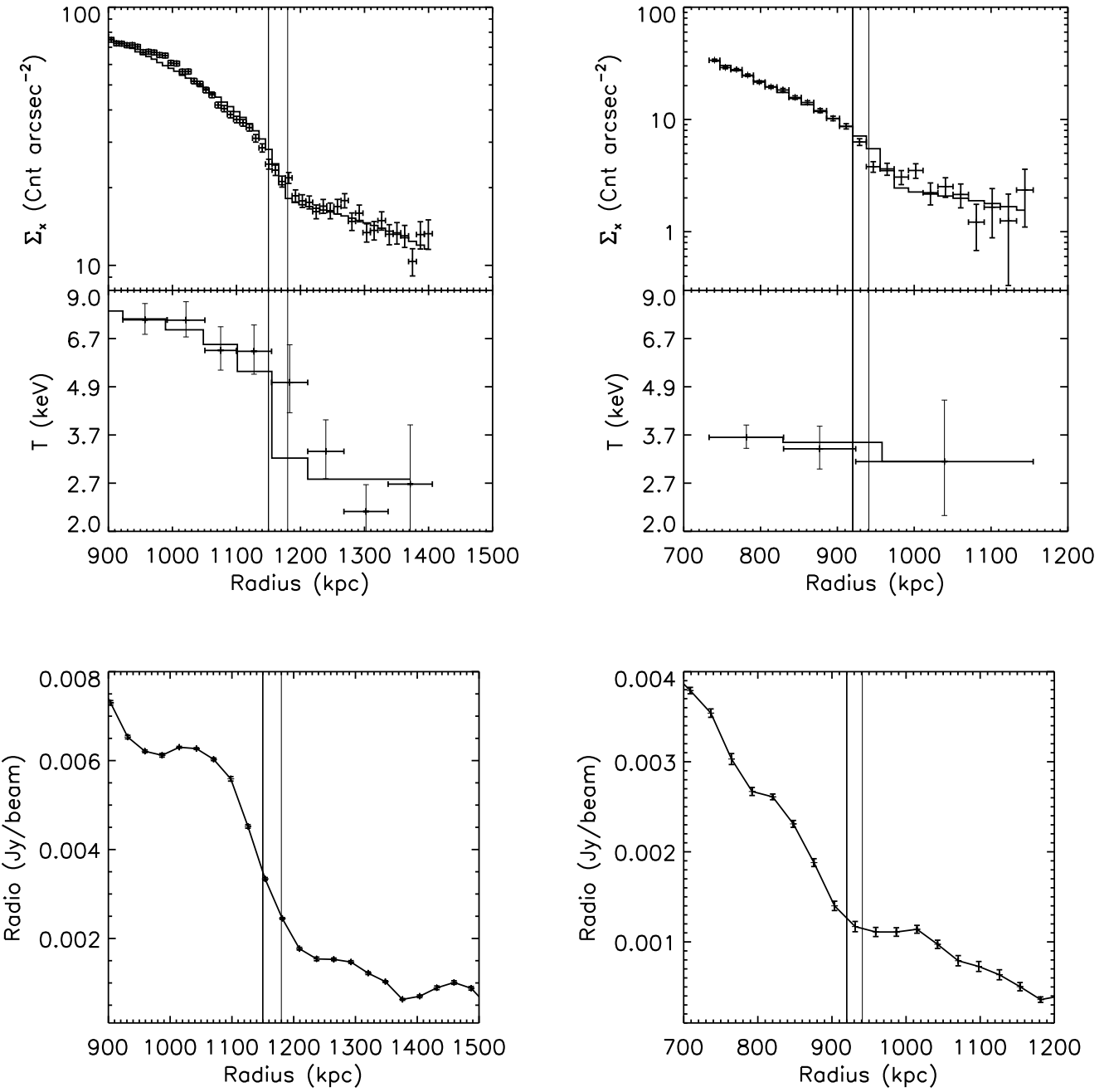


Fig. 15: Comparison of the X-ray and radio properties in the west (left column) and southeast (right column) sectors. *Upper panel*: Surface brightness and temperature profiles of the *XMM-Newton* mosaic. The continuous histograms show the best fit projected density and temperature discontinuous models to the data. The 3D pressure model is overplotted in Fig. 7. *Lower panel*: Radial profiles of 352 MHz radio emission at 2 arcmin resolution in the west (left) and southeast (right) sectors, after subtraction of radio emission from compact sources (see Brown & Rudnick 2011). The two vertical lines mark the position range of the jumps.

The X-ray surface brightness and temperature profiles have been derived from the *XMM-Newton* mosaic while the radio profile is extracted from the Westerbork observations at 352 MHz at 2 arcmin resolution. To guide the reader's eye, we mark, for each profile in the figure, the position of the pressure jump as derived from the analysis of the  $y$  signal (See Table 3). For both sectors we find that the X-ray surface brightness and radio profiles show relatively sharp features at the same position as the steepening

of the *Planck*  $y$  profiles. This is also the case for the temperature profile of the west sector. For the southeast sector, however, this evidence is less clear. Because it is located in a much lower signal-to-noise region of the cluster, the error of the outermost temperature bin is too large to be able to put a stringent constraint on a possible temperature jump.

To check if the X-ray features are also consistent with the hypothesized presence of a discontinuity in the cluster pressure

Table 4: Main parameters of the fit of the temperature and density models to the *XMM-Newton* data (see Eq. 8 and Eq. 8). The symbols  $M_n$ ,  $M_T$ ,  $M_{nT}$ , and  $M_{SZ}$  represent the Mach numbers derived from the X-ray density, temperature, and pressure ( $n \times T$ ), and SZ pressure jumps, respectively (see text).

Sector	$r_x$ (Mpc)	$D_n$	$M_n$	$D_T$	$M_T$	$D_n \times D_T$	$M_{nT}$	$M_{SZ}$
West	$1.173^{+0.0003}_{-0.003}$	$2.00^{+0.03}_{-0.03}$	$1.73^{+0.03}_{-0.03}$	$3.0^{+0.7}_{-0.6}$	$2.6^{+0.4}_{-0.4}$	$6.0^{+1.4}_{-1.1}$	$2.3^{+0.2}_{-0.2}$	$1.95^{+0.45}_{-0.02}$
Southeast	$0.9778^{+0.0002}_{-0}$	$2.43^{+0.02}_{-0.02}$	$2.10^{+0.01}_{-0.01}$	$1.3^{+1.8}_{-0.6}$	$1.3^{+1.3}_{-1.3}$	$3.1^{+1.6}_{-1.1}$	$1.6^{+0.3}_{-0.1}$	$2.03^{+0.14}_{-0.04}$

profile we simultaneously fit the observed X-ray surface brightness and temperature profiles using the following discontinuous 3D density and temperature models:

$$n = n_0 \times \begin{cases} D_n(r/r_X)^{-\xi_1} & r < r_X \\ (r/r_X)^{-\xi_2} & r > r_X, \end{cases} \quad (8)$$

and

$$T = T_0 \times \begin{cases} D_T(r/r_X)^{-\zeta_1} & r < r_X \\ (r/r_X)^{-\zeta_2} & r > r_X, \end{cases} \quad (9)$$

where  $r_X$  is the position of the X-ray jump and  $D_n$  and  $D_T$  are amplitudes of the density and temperature discontinuities, respectively. The above models are projected along the line of sight for  $r < 10$  Mpc using a temperature function appropriate for spectroscopic data (Mazzotta et al. 2004). Notice that due to the poor statistics of the temperature in the southeast sector, for this profile we fix  $\xi_1 = \xi_2 = 0$ . This choice does not affect the determination of the jump position  $r_X$  which is mainly driven by the surface brightness rather than by the temperature profile.

The best-fit position, density, and temperature jumps together with their 68% confidence level errors are reported in Table 4. To make a direct comparison with the pressure jump measured from the SZ signal, in the same table we add the amplitude of the X-ray pressure jump derived by multiplying the X-ray density and temperature models ( $P_x = n_x T$ ).

The best-fit surface brightness and projected temperature models are shown as histograms in Fig. 15. The best fit 3D  $P_x$  model and its 68% confidence level errors are overplotted in Fig. 7.

From Table 4 we see that the X-ray data from the west sector are consistent with the presence of a discontinuity both in the 3D density and 3D temperature profiles. Both jumps are detected at  $> 5\sigma$  confidence level and the pressure jumps derived from X-ray and from SZ are consistent within the 68% confidence level errors (Table 3 and Table 4). This agreement near the discontinuity is also illustrated by Fig. 7 which, in addition, shows that the 3D pressure profiles for the west sector derived from the SZ and the X-ray data are consistent not only near the jump but also over a much wider radial range.

These results indicate that the feature seen by *Planck* is produced by a shock induced by supersonic motions in the cluster's hot gas atmosphere. Assuming Rankine-Hugoniot pressure jump conditions across the fronts the discontinuity in the density, temperature and pressure profiles are uniquely linked to the shock Mach number.

Table 4 shows that, consistent with the amplitude of the pressure jumps, the Mach number obtained from the SZ and X-ray pressure profiles are consistent within the  $1\sigma$  confidence level errors. Furthermore, the Mach number derived from the X-ray density and temperature profiles agree within the  $2\sigma$  confidence level errors. This agreement supports the hypothesis that the west feature observed by *Planck* is a shock front.

For the southeast sector Table 4 shows that the X-ray surface brightness profile is consistent with the presence of a significant discontinuity in the 3D density profile. Due to the low statistics, the temperature model returns large errors and  $D_T$  is not constrained (see Table 4). Thus, although consistent, we cannot confirm the presence of a temperature jump. Despite this we find that, as for the west sector, the pressure jumps and the pressure profiles derived from X-ray and from SZ are consistent within the 68% confidence level errors (see Fig. 7, Table 3, and Table 4). Finally, Table 4 shows that the Mach numbers derived from the amplitudes of the different 3D models are all consistent within the 68% uncertainties level. We would like to stress that this is true not only for  $M_T$  and  $M_{nT}$  which, being directly connected to  $D_T$ , have relatively large errors, but also for  $M_n$  and  $M_{SZ}$  which do not depends on  $D_T$  at all. As for the west sector, this agreement supports the initial hypothesis that the southwest feature observed by *Planck* is also a shock front.

Notice that the good agreement between the 3D pressure models derived from the X-ray and SZ data, both in the west and southeast sectors, indicate that, within the selected sectors, spherical symmetry is a good approximation to the underlying pressure distribution.

We conclude this section by pointing the reader's attention to the fact that, even though the radio and X-ray observations have a much better PSF than *Planck*, Fig. 15 shows that the respective jumps in these observations appear smooth on a scale of  $\approx 200$  kpc  $\approx 7'$ . As explained in detail in Appendix A this is simply a projection effect. Despite its relatively large PSF, *Planck* is able to measure pressure jumps in the atmosphere of the Coma cluster as well as the other techniques.

#### 9.4. Quasi-linear SZ-radio relation

In Section 8 we show that for the Coma cluster the radio brightness and  $y$  emission scale approximately linearly with a small scatter between the radio emission and thermal pressure. Due to the near-linear correlation, where line-of-sight projection effects cancel out, we work here with volume-averaged emissivities. We first express the monochromatic radio emissivity [ $\text{erg s}^{-1} \text{cm}^{-3} \text{str}^{-1} \text{Hz}^{-1}$ ] as:

$$\epsilon_r \sim n_{\text{CRe}} B^{1+\alpha} \sim Q_{\text{CRe}} \frac{B^{1+\alpha}}{B^2 + B_{\text{CMB}}^2}, \quad (10)$$

where  $\alpha$  is the spectral index,  $B$  is the magnetic field,  $B_{\text{CMB}} \approx 3(1+z) \mu\text{G}$  is the equivalent magnetic field of the CMB, and  $n_{\text{CRe}}$  and  $Q_{\text{CRe}}$  are the density and injection rate of cosmic-ray electrons (CRe), respectively. In general,  $Q_{\text{CRe}}$  can be a function of position and electron energy, and will depend on the model of cosmic-ray acceleration assumed. In secondary (hadronic) acceleration models Dennison (1980); Vestrand (1982), the relativistic electrons are produced in collisions of long-lived

cosmic ray protons with the thermal electrons, resulting in  $Q_{\text{CRe}} \propto n_{\text{thermal}} n_{\text{CRp}}$ , where  $n_{\text{CRp}}$  is the density of cosmic-ray protons. Recent models in this category (Keshet & Loeb 2010; Keshet et al. 2010) require that, in contrast to  $n_{\text{thermal}}$ ,  $n_{\text{CRp}}$  should be constant over the cluster volume in order to match the cluster radio brightness profiles. Pfrommer et al. (2008) show that there is strong CRp injection even in the cluster peripheries, due to the stronger shock waves there. Strong radio CRp diffusion and streaming within the ICM could also lead to a completely flat CRp profile (Enßlin et al. 2011). In the limit where  $B \gg B_{\text{CMB}}$  and assuming  $\alpha \approx 1$  (e.g. Giovannini et al. 1993; Deiss et al. 1997), this would lead to  $\epsilon_r \propto n_{\text{thermal}} \propto y/T$ . This is consistent with our observations<sup>3</sup>, especially since  $n_{\text{thermal}}(r)$  varies much more than  $T(r)$  in the Coma cluster (see e.g. Arnaud et al. 2001; Snowden et al. 2008). Jeltema & Profumo (2011) derive a lower limit for the average field in Coma of  $1.7 \mu\text{G}$ , from limits on the *Fermi*  $\gamma$ -ray flux. The  $\gamma$ -ray analysis thus leaves open the question of whether Coma could be in the strong-field limit.

However, the rotation measure observations of Bonafede et al. (2010) provide characteristic values of  $4\text{-}5 \mu\text{G}$  for the combined contributions of the central diffuse cluster field and contributions local to each radio source (e.g. Guidetti et al. 2011; Rudnick & Blundell 2003). The majority of Coma's volume, which is outside of the cluster core, is thus in the weak-field limit, which leads to  $\epsilon_r \propto y B^2/T$ . To remain consistent with the linear correlation found here, the magnetic field would thus need to be nearly independent of thermal density. The non-ideal MHD simulations of Bonafede et al. (2011) show a typical scaling of  $B \propto n_{\text{thermal}}^{0.6}$ , which would yield  $\epsilon_r \propto y^{2.2}/T^{2.2}$ . This could make the secondary model inconsistent with the observations in the weak-field limit.

Primary (re-)acceleration models assume that relativistic electrons are accelerated directly from shocks and/or turbulence generated in cluster mergers. The turbulent re-acceleration model (Schlickeiser et al. 1987; Brunetti et al. 2001; Petrosian 2001) leads to a scaling of  $\epsilon_r \propto n_{\text{thermal}} T^{1.5} \propto y \sqrt{T}$  in the  $B < B_{\text{CMB}}$  limit (Cassano et al. 2007) if one assumes  $B^2 \propto n_{\text{thermal}}$  which is close to the simulation scaling results of Bonafede et al. (2011). Such a scaling relation is consistent with the observed correlation. However, in order to connect the CRe density to  $n_{\text{thermal}}$ , primary models depend on a large number of free parameters, which are generally fit to match the observations. Recent attempts to reduce the number of assumptions by introducing secondary CRe $^\pm$  as seed particles (Brunetti & Lazarian 2011, , see above) fail to reproduce the linear correlation in the weak-field limit. This is another manifestation of the problem all simple models have in explaining the large extent of cluster radio profiles when compared to the X-rays and inferred magnetic fields (e.g., Dolag & Enßlin 2000; Govoni et al. 2001; Donnert et al. 2010; Brown & Rudnick 2011). In future, robust measurements of the cluster's magnetic field profile, coupled with high-resolution radio/X-ray/SZ correlations, will be needed to rule out these naive models.

<sup>3</sup> In the case that  $\alpha = 1 + \delta$ , the relationship would be  $\epsilon_r \propto (y/T)^{1+\delta/2}$ , if we assume  $B \propto \sqrt{n_{\text{thermal}}}$ . E.g., if we use  $\alpha = 1.2$  (Giovannini et al. 1993), we would expect  $y \propto T_{\epsilon_r}^{0.91}$ , which is approximately our measured value. However, we continue to use the term "linear relationship", with the understanding that the difference between our measured value and linear is consistent for our simple assumption about the spectral index.

## 9.5. Pressure jumps and radio emission

Shocks play an important role in the production of radio emission. We expect that shocks created during cluster mergers will compress magnetic fields and accelerate relativistic particles. However, the radiating electrons will quickly lose their energy post-shock, and may not be visible for more than  $\sim 100$  kpc behind the shock (e.g., Markevitch et al. 2005) given characteristic shock velocities and magnetic fields at  $\mu\text{G}$  levels. These shock-accelerated electrons, in shock-compressed magnetic fields, have been proposed as the explanation for the observed polarized radio synchrotron radiation from cluster peripheral relic sources (Ensslin et al. 1998). Lower fields do not increase the electron lifetimes, and can even decrease them at fixed observing frequency, because of inverse Compton losses against the CMB. Recent simulations show that the presence of cluster-wide turbulence following a major merger is maintained for a few Gyr at a few percent thermal pressure (e.g., Dolag et al. 2005; Vazza et al. 2006; Kang et al. 2007; Paul et al. 2011). This turbulence can re-accelerate mildly relativistic seed electrons, and is potentially responsible for the large-scale halo emission (see above). In addition, an extensive population of low Mach number shocks is also seen in simulations (e.g., Miniati et al. 2000; Pfrommer et al. 2006) and could play an important role in particle re-acceleration.

Shocks will also induce turbulence in the post-shock region ( $\sim 200\text{-}300$  kpc). There are hints from the small-scale X-ray residuals (Fig. 3 of Schuecker et al. (2004)) that such turbulence may exist interior to the possible shocks seen in the west and southeast. For the western region, the combination of SZ/X-ray pressure jump, X-ray suggested turbulence, and excess synchrotron emission, points toward a connection between turbulence and diffuse synchrotron emission. The details of that connection, however, are not clear. In addition to direct acceleration by turbulence, the post-shock synchrotron emission could be a result of a population of weaker, as yet undetected shocks, or freshly accelerated CRp interacting with the ICM in a region where turbulence has amplified the magnetic field (e.g., Dolag et al. 2005; Ryu et al. 2008; Kushnir et al. 2009; Keshet 2010). Synchrotron spectral indices and magnetic field measurements, in combination with reliable measurements of weaker shocks and turbulence, would be needed to discriminate between potential models.

The expected rapid loss of radio emissivity post-shock can also help us understand why shocks are sometimes easily detected in the radio, and sometimes not. In the clearest cases, radio shocks are seen beyond any central halo as relatively thin structures known as peripheral relics (van Weeren et al. 2010) where they can accelerate relativistic electrons. Radio shocks may also be found at or near the edge of the halo, and would be characterized by a sharp, but low contrast, rise in brightness, while the post-shock emission blends in with the halo instead of falling off. The western shock described here in Coma, as well as suggested shocks at the edges of halos in Abell clusters 521 and 754 (Giacintucci et al. 2008; Markevitch 2010; Macario et al. 2011) are likely examples of this case. Contrast effects will camouflage the appearance of shocks that are projected against any radio halo emission. This is probably the case for the  $y$  shock in the southeast, where the radio halo extends far beyond the shock. The Coma cluster thus hosts all three types of "radio shocks": a) the classic *peripheral relic* at a distance of  $1.7 \text{ Mpc}$  from the center (which Ensslin et al. 1998 and Brown & Rudnick 2011 suggest is an "infall" shock), b) the western shock at the *edge* of the halo, and c) the southeast shock

projected against the fading radio halo.

## 10. Conclusions

We present the SZ observations of the Coma cluster based on the *Planck* nominal survey of 14 months. The excellent sensitivity of *Planck* allows, for the first time, the detection of SZ emission out to at least  $R \approx 3 \times R_{500}$ . We limit our investigation to the radial and sectoral properties of the intracluster medium, and we study the pressure distribution to the outermost cluster regions. Our three main results can be summarized as follows:

- the Coma pressure profile is flatter than the mean pressure profile predicted by the B04+N07+P08 numerical simulations and lies on the upper envelope of this specific simulated profile distribution. This trend has also been found in the pressure profile derived by stacking 62 nearby clusters of galaxies observed with *Planck* (Planck Collaboration V 2012).
- *Planck* detects a localised steepening of the  $y$  profile about half a degree to the west and also to the southeast of the cluster centre. Features in the X-ray and radio synchrotron profiles at similar locations suggest the presence of shock waves that propagate with Mach number  $M_w = 1.95^{+0.45}_{-0.02}$  and  $M_{se} = 2.03^{+0.14}_{-0.04}$  in the west and southeast directions, respectively.
- the  $y$  and radio-synchrotron signals are quasi-linearly correlated on Mpc-scales with only small intrinsic scatter. This implies either that, unlike the thermal plasma, the energy density of cosmic-ray electrons is relatively constant throughout the cluster, or that the magnetic fields fall off much more slowly with radius than previously thought. We detect a correspondence between the western  $y$  shock and previously reported radio/X-ray edge, and we argue that either the magnetic fields are strong in the cluster outskirts, which would permit the hadronic model to explain the radio emission, or some sort of re-acceleration by turbulence or additional shock waves must operate in the region behind the detected outer shock structures.

Even though this analysis is based on only about half of the data collected by *Planck*, our results represent a substantial step forward in the study of the physics of the Coma cluster. The full set of data collected by *Planck*, will not only improve the signal-to-noise by another factor  $\sim \sqrt{2}$  but also significantly improve our understanding of instrumental effects. Thus, we will be able to generate more accurate  $y$  maps, and more thoroughly unveil Coma's two-dimensional SZ structure and its filamentary environment.

**Acknowledgements.** A description of the Planck Collaboration and a list of its members, indicating which technical or scientific activities they have been involved in, can be found at [http://www.rssd.esa.int/Planck\\_Collaboration](http://www.rssd.esa.int/Planck_Collaboration). The Planck Collaboration acknowledges the support of: ESA; CNES and CNRS/INSU-IN2P3-INP (France); ASI, CNR, and INAF (Italy); NASA and DoE (USA); STFC and UKSA (UK); CSIC, MICINN and JA (Spain); Tekes, AOf and CSC (Finland); DLR and MPG (Germany); CSA (Canada); DTU Space (Denmark); SER/SSO (Switzerland); RCN (Norway); SFI (Ireland); FCT/MCTES (Portugal); and DEISA (EU). Partial support for this work for L. Rudnick comes from U.S. NSF Grant 09-08668 to the University of Minnesota. We would also like to acknowledge useful conversations with Gf. Brunetti.

## References

- Arnaud, M., Pratt, G. W., Piffaretti, R., et al. 2010, A&A, 517, A92  
 Basu, K. 2012, MNRAS, 421, L112  
 Battaglia, N., Bond, J. R., Pfrommer, C., & Sievers, J. L. 2011, eprint arXiv:1109.3709  
 Bersanelli, M., Mandolesi, N., Butler, R. C., et al. 2010, A&A, 520, A4+  
 Bobin, J., Moudden, Y., Starck, J.-L., Fadili, J., & Aghanim, N. 2008, Statistical Methodology, 5, 307  
 Bonafe, A., Dolag, K., Stasyszyn, F., Murante, G., & Borgani, S. 2011, MNRAS, 418, 2234  
 Bonafe, A., Feretti, L., Murgia, M., et al. 2010, A&A, 513, A30  
 Bonamente, M., Joy, M. K., & Lieu, R. 2003, ApJ, 585, 722  
 Bonamente, M., Lieu, R., & Bulbul, E. 2009, ApJ, 696, 1886  
 Borgani, S., Murante, G., Springel, V., et al. 2004, MNRAS, 348, 1078  
 Bourdin, H., Arnaud, M., Mazzotta, P., et al. 2011, A&A, 527, A21+  
 Bourdin, H., & Mazzotta, P. 2008, A&A, 479, 307  
 Briel, U. G., Henry, J. P., & Boehringer, H. 1992, A&A, 259, L31  
 Brown, S. & Rudnick, L. 2011, MNRAS, 412, 2  
 Brunetti, G. & Lazarian, A. 2011, MNRAS, 410, 127  
 Brunetti, G., Setti, G., Feretti, L., & Giovannini, G. 2001, MNRAS, 320, 365  
 Cassano, R., Brunetti, G., Setti, G., Govoni, F., & Dolag, K. 2007, MNRAS, 378, 1565  
 Churazov, E., Vikhlinin, A., Zhuravleva, I., et al. 2012, MNRAS, 2290  
 De Petris, M., D'Alba, L., Lamagna, L., et al. 2002, ApJ, 574, L119  
 Deiss, B. M., Reich, W., Lesch, H., & Wielebinski, R. 1997, A&A, 321, 55  
 Dennison, B. 1980, ApJ, 239, L93  
 Dolag, K. & Enßlin, T. A. 2000, A&A, 362, 151  
 Dolag, K., Vazza, F., Brunetti, G., & Tormen, G. 2005, MNRAS, 364, 753  
 Donnert, J., Dolag, K., Cassano, R., & Brunetti, G. 2010, MNRAS, 407, 1565  
 Dow, K. L. & White, S. D. M. 1995, ApJ, 439, 113  
 Enßlin, T., Pfrommer, C., Miniati, F., & Subramanian, K. 2011, A&A, 527, A99  
 Enßlin, T. A., Biermann, P. L., Klein, U., & Kohle, S. 1998, A&A, 332, 395  
 Eriksen, H. K., Banday, A. J., Górski, K. M., & Lilje, P. B. 2004, ApJ, 612, 633  
 Giacintucci, S., Venturi, T., Macario, G., et al. 2008, A&A, 486, 347  
 Giovannini, G., Feretti, L., Venturi, T., Kim, K.-T., & Kronberg, P. P. 1993, ApJ, 406, 399  
 Górski, K. M., Hivon, E., Banday, A. J., et al. 2005, ApJ, 622, 759  
 Govoni, F., Enßlin, T. A., Feretti, L., & Giovannini, G. 2001, A&A, 369, 441  
 Guidetti, D., Laing, R. A., Bridle, A. H., Parma, P., & Gregorini, L. 2011, MNRAS, 413, 2525  
 Herbig, T., Lawrence, C. R., Readhead, A. C. S., & Gulkis, S. 1995, ApJ, 449, L5  
 Herbig, T., Readhead, A. C. S., & Lawrence, C. R. 1992, in Bulletin of the American Astronomical Society, Vol. 24, American Astronomical Society Meeting Abstracts, 1263  
 Hurier, G., Hildebrandt, S. R., & Macias-Perez, J. F. 2010, ArXiv e-prints  
 Jeltema, T. E. & Profumo, S. 2011, ApJ, 728, 53  
 Kang, H., Ryu, D., Cen, R., & Ostriker, J. P. 2007, ApJ, 669, 729  
 Kelly, B. C. 2007, ApJ, 665, 1489  
 Keshet, U. 2010, ArXiv e-prints  
 Keshet, U. & Loeb, A. 2010, ApJ, 722, 737  
 Keshet, U., Markevitch, M., Birnboim, Y., & Loeb, A. 2010, ApJ, 719, L74  
 Komatsu, E., Smith, K. M., Dunkley, J., et al. 2011, ApJS, 192, 18  
 Kushnir, D., Katz, B., & Waxman, E. 2009, J. Cosmology Astropart. Phys., 9, 24  
 Lamarre, J., Puget, J., Ade, P. A. R., et al. 2010, A&A, 520, A9+  
 Lancaster, K., Genova-Santos, R., Falcón, N., et al. 2005, MNRAS, 359, 16  
 Leahy, J. P., Bersanelli, M., D'Arcangelo, O., et al. 2010, A&A, 520, A8+  
 Macario, G., Markevitch, M., Giacintucci, S., et al. 2011, ApJ, 728, 82  
 Malu, S. S. & Subrahmanyam, R. 2012, Journal of Astrophysics and Astronomy, 20  
 Mandolesi, N., Bersanelli, M., Butler, R. C., et al. 2010, A&A, 520, A3+  
 Markevitch, M. 2010, ArXiv e-prints  
 Markevitch, M., Govoni, F., Brunetti, G., & Jerius, D. 2005, ApJ, 627, 733  
 Mazzotta, P., Rasia, E., Moscardini, L., & Tormen, G. 2004, MNRAS, 354, 10  
 Meneghetti, M., Rasia, E., Merten, J., et al. 2010, A&A, 514, A93  
 Mennella et al. 2011, A&A, 536, A3  
 Miniati, F., Ryu, D., Kang, H., et al. 2000, ApJ, 542, 608  
 Nagai, D., Vikhlinin, A., & Kravtsov, A. V. 2007, ApJ, 655, 98  
 Neumann, D. M., Arnaud, M., Gastaud, R., et al. 2001, A&A, 365, L74  
 Neumann, D. M., Lumb, D. H., Pratt, G. W., & Briel, U. G. 2003, A&A, 400, 811  
 Paul, S., Iapichino, L., Miniati, F., Bagchi, J., & Mannheim, K. 2011, ApJ, 726, 17  
 Petrosian, V. 2001, ApJ, 557, 560  
 Pfrommer, C., Enßlin, T. A., & Springel, V. 2008, MNRAS, 385, 1211  
 Pfrommer, C., Springel, V., Enßlin, T. A., & Jubelgas, M. 2006, MNRAS, 367, 113  
 Piffaretti, R. & Valdarnini, R. 2008, A&A, 491, 71

- Planck Collaboration. 2011a, A&A, 536, A1  
 Planck Collaboration. 2011b, A&A, 536, A2  
 Planck Collaboration. 2011c, A&A, 536, A9  
 Planck Collaboration. 2011d, A&A, 536, A8  
 Planck Collaboration. 2011e, A&A, 536, A10  
 Planck HFI Core Team. 2011a, A&A, 536, A4  
 Planck HFI Core Team. 2011b, A&A, 536, A6  
 Planck Collaboration V. 2012, Planck Intermediate results. V. Pressure profiles of galaxy clusters from the Sunyaev-Zeldovich effect. (Submitted to A&A, arXiv : astro-ph/1207.4061 )  
 Remazeilles, M., Delabrouille, J., & Cardoso, J.-F. 2011, MNRAS, 410, 2481  
 Rosset, C., Tristram, M., Ponthieu, N., et al. 2010, A&A, 520, A13+  
 Rudnick, L. & Blundell, K. M. 2003, ApJ, 588, 143  
 Ryu, D., Kang, H., Cho, J., & Das, S. 2008, Science, 320, 909  
 Sarazin, C. L. 1999, ApJ, 520, 529  
 Schlickeiser, R., Sievers, A., & Thiemann, H. 1987, A&A, 182, 21  
 Schuecker, P., Finoguenov, A., Miniati, F., Böhringer, H., & Briel, U. G. 2004, A&A, 426, 387  
 Silverberg, R. F., Cheng, E. S., Cottingham, D. A., et al. 1997, ApJ, 485, 22  
 Snowden, S. L., Mushotzky, R. F., Kuntz, K. D., & Davis, D. S. 2008, A&A, 478, 615  
 Tauber, J. A., Mandolesi, N., Puget, J., et al. 2010, A&A, 520, A1+  
 van Weeren, R. J., Röttgering, H. J. A., Brüggen, M., & Hoeft, M. 2010, Science, 330, 347  
 Vazza, F., Tormen, G., Cassano, R., Brunetti, G., & Dolag, K. 2006, MNRAS, 369, L14  
 Vestrand, W. T. 1982, AJ, 87, 1266  
 Vikhlinin, A., Forman, W., & Jones, C. 1997, ApJ, 474, L7  
 Vikhlinin, A., Kravtsov, A., Forman, W., et al. 2006, ApJ, 640, 691  
 White, S. D. M., Briel, U. G., & Henry, J. P. 1993, MNRAS, 261, L8  
 Zacchei et al. 2011, A&A, 536, A5

## Appendix A: Pressure profile discontinuities as seen by *Planck*

In this section we show that the 10 arcmin angular resolution of *Planck* is still sufficient to detect and measure 3D pressure jump features in the Coma cluster. This is because at the cluster redshift, 10 arcmin  $\approx$  280 kpc, which is of the order of the smoothing induced by projection. To show this, we assume a discontinuous 3D pressure profile described by Eq. 6. We project this profile along the line of sight and we calculate the corresponding  $y$  profile as observed with an instrument with

- i) infinite angular resolution;
- ii) a 10' FWHM angular resolution, as for *Planck*.

The results of this exercise are illustrated in Fig. A.1 where we compare four different cases with and without pressure jumps. In the upper section of each panel of Fig. A.1 we show the input 3D pressure profiles. In the middle sections we show the projected pressure profiles without any smoothing (as black histograms). The lower sections show deviations from a single power-law fit. The panel on the left shows that, due to simple projection effects, the  $y$  profile appears smoothed with an equivalent smoothing scale of  $\approx 200 - 250$  kpc. For Coma, this corresponds to an angular scale of 7 – 9 arcmin. In the same panel we overplot, as a red histogram, the  $y$  profile convolved with the *Planck* PSF. This illustrates that the effect of the PSF smoothing is secondary with respect to projection effects. This indicates that there is only a modest gain, from the detection point of view, in observing this specific feature using an instrument with a much better angular resolution than *Planck*. Notice that the fact that the projection of the 3D pressure distribution onto a plane converts the sharp jump into a curved surface brightness profile allows us to recover the position of  $r_J$  with an accuracy higher than the angular resolution of *Planck*.

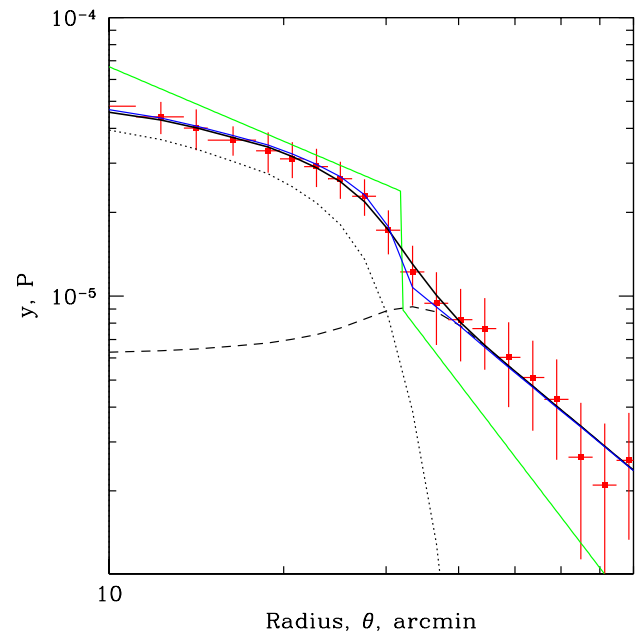


Fig. A.2: Comparison of the 3D pressure model (green line) and the corresponding projected  $y$  profile, smoothed with the 10' beam. The dotted black line shows the expected  $y$  profile due to the inner power component, while the dashed line shows the contribution of the outer power-law component. The black solid line is the sum of these two components. For comparison, the blue line shows the same model, but not convolved with the 10' beam. In this plot  $r_J \sim 30'$ . Due to projection effects, the range of radii affected by the value of  $r_J$  is of order  $r_J$  itself. Since  $r_J$  exceeds 10', many independent data points with large signal-to-noise ratio contributes to the determination of  $r_J$ , allowing  $r_J$  to be estimated with an uncertainty below the nominal angular resolution of the telescope.

Fig. A.2 clearly shows that the range of radii affected by  $r_J$  value is of the order of  $r_J$  itself. Since  $r_J > 10'$ , many independent data points with large signal-to-noise ratio are contributing to the determination of  $r_J$ , driving the uncertainty well below the nominal angular resolution of the telescope. Of course the value of  $r_J$  is still subject to systematic uncertainties, e.g. from our assumption of spherical symmetry.

We use the above exercise to illustrate two practical ways to identify the presence of a possible underlying 3D discontinuous pressure profile, hidden behind some observed projected profile extracted in a specific cluster sector.

The first way is to search for the actual pressure jump in the observed pressure profile. As projection smooths the profile, this needs to be done by looking at the profile extremes. We first notice that the outermost bins of the profile are practically unaffected by PSF smoothing. This is clear in the middle sections of Fig. A.1 where the red and black histograms are similar in the outermost 3-4 bins. At this point, if we fit a line to the observed 3-4 outermost bins, this will give an indication of the un-convolved  $y$  profile slope at large radii. If we extrapolate this line to the center, we can easily highlight the presence of a pressure jump. This procedure is shown in the middle section of Fig. A.1 with black straight lines. From Fig. A.1 we can see

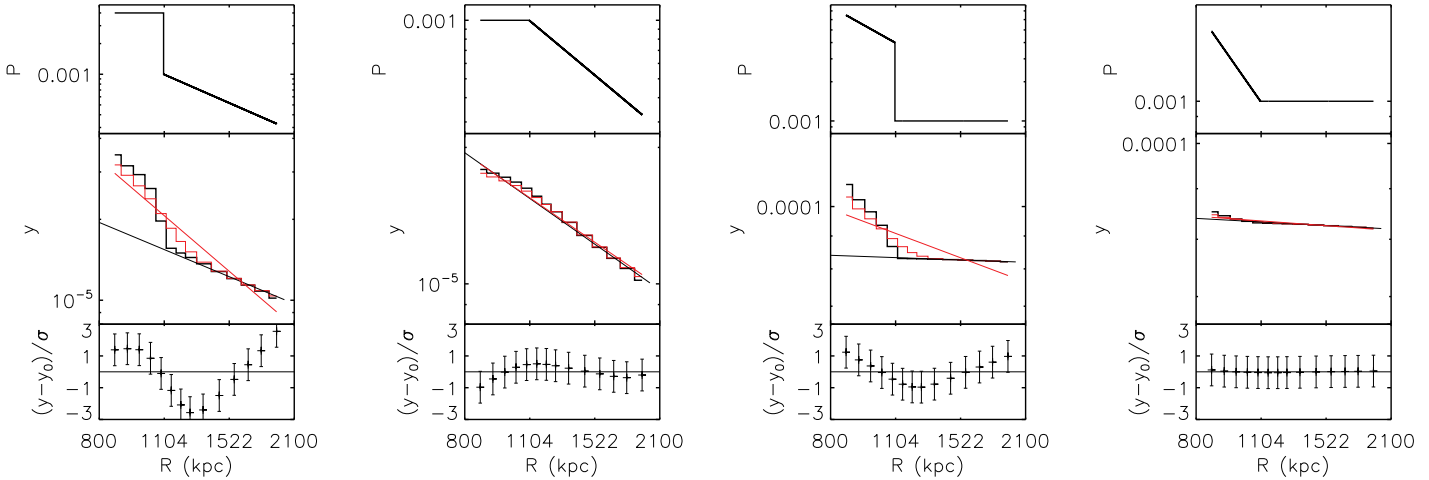


Fig. A.1: Illustration of the effect induced by projection and by the *Planck* PSF on the  $y$  radial profile produced by an underlying broken power-law pressure profile with and without a pressure discontinuity. In this figure we fix  $P_0 = 10 \times 10^{-4} \text{ cm}^{-3} \text{ keV}$ ,  $r_J = 1.1 \text{ Mpc}$  and, from left to right we consider four different cases: i)  $\eta_1 = 0$ ,  $\eta_2 = 2$ ,  $D_J = 4$ ; ii)  $\eta_1 = 0$ ,  $\eta_2 = 2$ ,  $D_J = 1$ ; iii)  $\eta_1 = 2$ ,  $\eta_2 = 0$ ,  $D_J = 4$ ; iv)  $\eta_1 = 2$ ,  $\eta_2 = 0$ ,  $D_J = 1$ . *Upper Panels*: The underlying 3D pressure profile; *Middle Panels*: The black and red histograms are the projected  $y$  profiles observed by an instrument with infinite angular resolution and with a PSF of 10 arcmin, respectively. The red line represents the best fit of a simple power-law to the entire convolved profile (red histogram). The black line is the same as the red line but considering only the three outermost projected profile bins. *Lower Panels*: Ratio between the PSF convolved and projected  $y$  profile and its best-fit power-law model (red histogram and lines in middle panel) in units of a relative error which, for this illustration, we set to 10%.

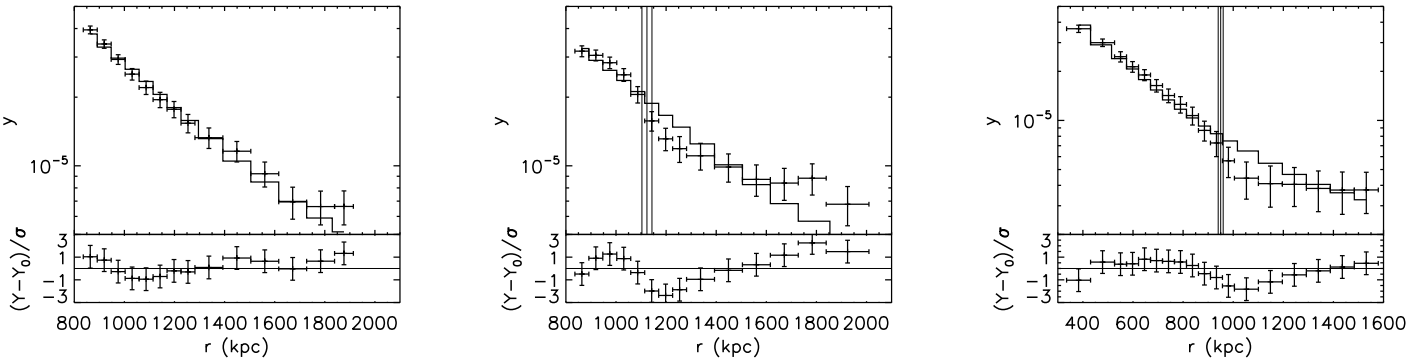


Fig. A.3: Results of the fit of the  $y$  profile extracted from three cluster sectors with a simple power-law. *Left Panel*) sector with the same angular size and extension as the west shock but pointing to the north, where there are no visible shock features; *Middle Panel*) profile of the west shock; *Right Panel*) profile of the southeast shock. In the lower panel of each figure we report the ratio between the observed and the best fit model of the projected  $y$  profile in units of the relative error. The figure clearly illustrates that while the power-law gives a good fit for the north sector where no shock is present, it returns a poor fit in the west and southeast sectors. These two cluster regions require a discontinuity in the pressure jump as shown in Fig. 6.

that, this procedure highlights the intensity variation due to a pressure jump (see first and third panels). In the case where we have no pressure jump (second and forth panels) the best-fit line to the outermost bins tends to closely follow the entire profile.

The second way to highlight the presence of a pressure jump is to fit a line to the entire observed profile and to examine the residuals. This procedure is illustrated in the middle and lower sections of Fig. A.1. The red lines in the middle section are the best fit power-law relations to the entire observed profile (red histogram). The crosses in the lower panels indicate the differences, in units of the relative errors, between the PSF convolved projected  $y$  profile and its best fit power-law model.

This figure shows that a 3D pressure jump induces a characteristic signature in the residuals.

In Fig. A.3 we apply this second technique to the Coma cluster by showing the fit of the  $y$  profile extracted from three cluster sectors with a simple power-law. The figure clearly illustrates that while the power-law gives a good fit for the north sector where no shock is present, it returns a poor fit in the west and southeast sectors. These two cluster regions require a discontinuity in the pressure jump as shown in Fig. 6.

<sup>1</sup> APC, AstroParticule et Cosmologie, Université Paris Diderot, CNRS/IN2P3, CEA/Irfu, Observatoire de Paris, Sorbonne Paris Cité, 10, rue Alice Domon et Léonie Duquet, 75205 Paris Cedex 13, France

- <sup>2</sup> Aalto University Metsähovi Radio Observatory, Metsähovintie 114, FIN-02540 Kylmälä, Finland
- <sup>3</sup> Agenzia Spaziale Italiana Science Data Center, c/o ESRIN, via Galileo Galilei, Frascati, Italy
- <sup>4</sup> Agenzia Spaziale Italiana, Viale Liegi 26, Roma, Italy
- <sup>5</sup> Astrophysics Group, Cavendish Laboratory, University of Cambridge, J J Thomson Avenue, Cambridge CB3 0HE, U.K.
- <sup>6</sup> Atacama Large Millimeter/submillimeter Array, ALMA Santiago Central Offices, Alonso de Cordova 3107, Vitacura, Casilla 763 0355, Santiago, Chile
- <sup>7</sup> CITA, University of Toronto, 60 St. George St., Toronto, ON M5S 3H8, Canada
- <sup>8</sup> CNRS, IRAP, 9 Av. colonel Roche, BP 44346, F-31028 Toulouse cedex 4, France
- <sup>9</sup> California Institute of Technology, Pasadena, California, U.S.A.
- <sup>10</sup> Centre of Mathematics for Applications, University of Oslo, Blindern, Oslo, Norway
- <sup>11</sup> Centro de Astrofísica, Universidade do Porto, Rua das Estrelas, 4150-762 Porto, Portugal
- <sup>12</sup> Centro de Estudios de Física del Cosmos de Aragón (CEFCA), Plaza San Juan, 1, planta 2, E-44001, Teruel, Spain
- <sup>13</sup> Computational Cosmology Center, Lawrence Berkeley National Laboratory, Berkeley, California, U.S.A.
- <sup>14</sup> Consejo Superior de Investigaciones Científicas (CSIC), Madrid, Spain
- <sup>15</sup> DSM/Irfu/SPP, CEA-Saclay, F-91191 Gif-sur-Yvette Cedex, France
- <sup>16</sup> DTU Space, National Space Institute, Technical University of Denmark, Elektrovej 327, DK-2800 Kgs. Lyngby, Denmark
- <sup>17</sup> Département de Physique Théorique, Université de Genève, 24, Quai E. Ansermet, 1211 Genève 4, Switzerland
- <sup>18</sup> Departamento de Física Fundamental, Facultad de Ciencias, Universidad de Salamanca, 37008 Salamanca, Spain
- <sup>19</sup> Departamento de Física, Universidad de Oviedo, Avda. Calvo Sotelo s/n, Oviedo, Spain
- <sup>20</sup> Department of Astrophysics, IMAPP, Radboud University, P.O. Box 9010, 6500 GL Nijmegen, The Netherlands
- <sup>21</sup> Department of Physics & Astronomy, University of British Columbia, 6224 Agricultural Road, Vancouver, British Columbia, Canada
- <sup>22</sup> Department of Physics and Astronomy, Dana and David Dornsife College of Letter, Arts and Sciences, University of Southern California, Los Angeles, CA 90089, U.S.A.
- <sup>23</sup> Department of Physics, Gustaf Hällströmin katu 2a, University of Helsinki, Helsinki, Finland
- <sup>24</sup> Department of Physics, Princeton University, Princeton, New Jersey, U.S.A.
- <sup>25</sup> Department of Physics, University of California, Berkeley, California, U.S.A.
- <sup>26</sup> Department of Physics, University of California, One Shields Avenue, Davis, California, U.S.A.
- <sup>27</sup> Department of Physics, University of California, Santa Barbara, California, U.S.A.
- <sup>28</sup> Department of Physics, University of Illinois at Urbana-Champaign, 1110 West Green Street, Urbana, Illinois, U.S.A.
- <sup>29</sup> Department of Statistics, Purdue University, 250 N. University Street, West Lafayette, Indiana, U.S.A.
- <sup>30</sup> Dipartimento di Fisica e Astronomia G. Galilei, Università degli Studi di Padova, via Marzolo 8, 35131 Padova, Italy
- <sup>31</sup> Dipartimento di Fisica, Università La Sapienza, P. le A. Moro 2, Roma, Italy
- <sup>32</sup> Dipartimento di Fisica, Università degli Studi di Milano, Via Celoria, 16, Milano, Italy
- <sup>33</sup> Dipartimento di Fisica, Università degli Studi di Trieste, via A. Valerio 2, Trieste, Italy
- <sup>34</sup> Dipartimento di Fisica, Università di Ferrara, Via Saragat 1, 44122 Ferrara, Italy
- <sup>35</sup> Dipartimento di Fisica, Università di Roma Tor Vergata, Via della Ricerca Scientifica, 1, Roma, Italy
- <sup>36</sup> Dipartimento di Matematica, Università di Roma Tor Vergata, Via della Ricerca Scientifica, 1, Roma, Italy
- <sup>37</sup> Discovery Center, Niels Bohr Institute, Blegdamsvej 17, Copenhagen, Denmark
- <sup>38</sup> Dpto. Astrofísica, Universidad de La Laguna (ULL), E-38206 La Laguna, Tenerife, Spain
- <sup>39</sup> European Southern Observatory, ESO Vitacura, Alonso de Cordova 3107, Vitacura, Casilla 19001, Santiago, Chile
- <sup>40</sup> European Space Agency, ESAC, Planck Science Office, Camino bajo del Castillo, s/n, Urbanización Villafranca del Castillo, Villanueva de la Cañada, Madrid, Spain
- <sup>41</sup> European Space Agency, ESTEC, Keplerlaan 1, 2201 AZ Noordwijk, The Netherlands
- <sup>42</sup> GEPI, Observatoire de Paris, Section de Meudon, 5 Place J. Janssen, 92195 Meudon Cedex, France
- <sup>43</sup> Helsinki Institute of Physics, Gustaf Hällströmin katu 2, University of Helsinki, Helsinki, Finland
- <sup>44</sup> INAF - Osservatorio Astrofisico di Catania, Via S. Sofia 78, Catania, Italy
- <sup>45</sup> INAF - Osservatorio Astronomico di Padova, Vicolo dell'Osservatorio 5, Padova, Italy
- <sup>46</sup> INAF - Osservatorio Astronomico di Roma, via di Frascati 33, Monte Porzio Catone, Italy
- <sup>47</sup> INAF - Osservatorio Astronomico di Trieste, Via G.B. Tiepolo 11, Trieste, Italy
- <sup>48</sup> INAF Istituto di Radioastronomia, Via P. Gobetti 101, 40129 Bologna, Italy
- <sup>49</sup> INAF/IASF Bologna, Via Gobetti 101, Bologna, Italy
- <sup>50</sup> INAF/IASF Milano, Via E. Bassini 15, Milano, Italy
- <sup>51</sup> INFN, Sezione di Roma 1, Università di Roma Sapienza, Piazzale Aldo Moro 2, 00185, Roma, Italy
- <sup>52</sup> INRIA, Laboratoire de Recherche en Informatique, Université Paris-Sud 11, Bâtiment 490, 91405 Orsay Cedex, France
- <sup>53</sup> IPAG: Institut de Planétologie et d'Astrophysique de Grenoble, Université Joseph Fourier, Grenoble 1 / CNRS-INSU, UMR 5274, Grenoble, F-38041, France
- <sup>54</sup> ISDC Data Centre for Astrophysics, University of Geneva, ch. d'Ecogia 16, Versoix, Switzerland
- <sup>55</sup> IUCAA, Post Bag 4, Ganeshkhind, Pune University Campus, Pune 411 007, India
- <sup>56</sup> Imperial College London, Astrophysics group, Blackett Laboratory, Prince Consort Road, London, SW7 2AZ, U.K.
- <sup>57</sup> Infrared Processing and Analysis Center, California Institute of Technology, Pasadena, CA 91125, U.S.A.
- <sup>58</sup> Institut Néel, CNRS, Université Joseph Fourier Grenoble I, 25 rue des Martyrs, Grenoble, France
- <sup>59</sup> Institut Universitaire de France, 103, bd Saint-Michel, 75005, Paris, France
- <sup>60</sup> Institut d'Astrophysique Spatiale, CNRS (UMR8617) Université Paris-Sud 11, Bâtiment 121, Orsay, France
- <sup>61</sup> Institut d'Astrophysique de Paris, CNRS (UMR7095), 98 bis Boulevard Arago, F-75014, Paris, France
- <sup>62</sup> Institute for Space Sciences, Bucharest-Magurale, Romania
- <sup>63</sup> Institute of Astro and Particle Physics, Technikerstrasse 25/8, University of Innsbruck, A-6020, Innsbruck, Austria
- <sup>64</sup> Institute of Astronomy and Astrophysics, Academia Sinica, Taipei, Taiwan
- <sup>65</sup> Institute of Astronomy, University of Cambridge, Madingley Road, Cambridge CB3 0HA, U.K.
- <sup>66</sup> Institute of Theoretical Astrophysics, University of Oslo, Blindern, Oslo, Norway
- <sup>67</sup> Instituto de Astrofísica de Canarias, C/Vía Láctea s/n, La Laguna, Tenerife, Spain
- <sup>68</sup> Instituto de Física de Cantabria (CSIC-Universidad de Cantabria), Avda. de los Castros s/n, Santander, Spain
- <sup>69</sup> Jet Propulsion Laboratory, California Institute of Technology, 4800 Oak Grove Drive, Pasadena, California, U.S.A.
- <sup>70</sup> Jodrell Bank Centre for Astrophysics, Alan Turing Building, School of Physics and Astronomy, The University of Manchester, Oxford Road, Manchester, M13 9PL, U.K.

- <sup>71</sup> Kapteyn Astronomical Institute, University of Groningen,  
Landleven 12, 9747 AD Groningen, The Netherlands
- <sup>72</sup> Kavli Institute for Cosmology Cambridge, Madingley Road,  
Cambridge, CB3 0HA, U.K.
- <sup>73</sup> LAL, Université Paris-Sud, CNRS/IN2P3, Orsay, France
- <sup>74</sup> LERMA, CNRS, Observatoire de Paris, 61 Avenue de  
l'Observatoire, Paris, France
- <sup>75</sup> Laboratoire AIM, IRFU/Service d'Astrophysique - CEA/DSM -  
CNRS - Université Paris Diderot, Bât. 709, CEA-Saclay, F-91191  
Gif-sur-Yvette Cedex, France
- <sup>76</sup> Laboratoire Traitement et Communication de l'Information, CNRS  
(UMR 5141) and Télécom ParisTech, 46 rue Barrault F-75634  
Paris Cedex 13, France
- <sup>77</sup> Laboratoire de Physique Subatomique et de Cosmologie,  
Université Joseph Fourier Grenoble I, CNRS/IN2P3, Institut  
National Polytechnique de Grenoble, 53 rue des Martyrs, 38026  
Grenoble cedex, France
- <sup>78</sup> Laboratoire de Physique Théorique, Université Paris-Sud 11 &  
CNRS, Bâtiment 210, 91405 Orsay, France
- <sup>79</sup> Lawrence Berkeley National Laboratory, Berkeley, California,  
U.S.A.
- <sup>80</sup> Max-Planck-Institut für Astrophysik, Karl-Schwarzschild-Str. 1,  
85741 Garching, Germany
- <sup>81</sup> Max-Planck-Institut für Extraterrestrische Physik,  
Giessenbachstraße, 85748 Garching, Germany
- <sup>82</sup> MilliLab, VTT Technical Research Centre of Finland, Tietotie 3,  
Espoo, Finland
- <sup>83</sup> National University of Ireland, Department of Experimental  
Physics, Maynooth, Co. Kildare, Ireland
- <sup>84</sup> Niels Bohr Institute, Blegdamsvej 17, Copenhagen, Denmark
- <sup>85</sup> Observational Cosmology, Mail Stop 367-17, California Institute  
of Technology, Pasadena, CA, 91125, U.S.A.
- <sup>86</sup> Optical Science Laboratory, University College London, Gower  
Street, London, U.K.
- <sup>87</sup> SISSA, Astrophysics Sector, via Bonomea 265, 34136, Trieste,  
Italy
- <sup>88</sup> School of Physics and Astronomy, Cardiff University, Queens  
Buildings, The Parade, Cardiff, CF24 3AA, U.K.
- <sup>89</sup> Space Research Institute (IKI), Russian Academy of Sciences,  
Profsoyuznaya Str, 84/32, Moscow, 117997, Russia
- <sup>90</sup> Space Sciences Laboratory, University of California, Berkeley,  
California, U.S.A.
- <sup>91</sup> Stanford University, Dept of Physics, Varian Physics Bldg, 382 Via  
Pueblo Mall, Stanford, California, U.S.A.
- <sup>92</sup> UPMC Univ Paris 06, UMR7095, 98 bis Boulevard Arago,  
F-75014, Paris, France
- <sup>93</sup> Universität Heidelberg, Institut für Theoretische Astrophysik,  
Albert-Überle-Str. 2, 69120, Heidelberg, Germany
- <sup>94</sup> Université Denis Diderot (Paris 7), 75205 Paris Cedex 13, France
- <sup>95</sup> Université de Toulouse, UPS-OMP, IRAP, F-31028 Toulouse cedex  
4, France
- <sup>96</sup> University Observatory, Ludwig Maximilian University of Munich,  
Scheinerstrasse 1, 81679 Munich, Germany
- <sup>97</sup> University of Granada, Departamento de Física Teórica y del  
Cosmos, Facultad de Ciencias, Granada, Spain
- <sup>98</sup> University of Miami, Knight Physics Building, 1320 Campo Sano  
Dr., Coral Gables, Florida, U.S.A.
- <sup>99</sup> Warsaw University Observatory, Aleje Ujazdowskie 4, 00-478  
Warszawa, Poland